

Vertically averaged and moment equations: New derivation, efficient numerical solution and comparison with other physical approximations for modeling non-hydrostatic free surface flows

C. Escalante^{a,*}, T. Morales de Luna^b, F. Cantero-Chinchilla^c, O. Castro-Organ^c

^a Dpto. de Matemática Aplicada, Universidad de Málaga, Málaga, Spain

^b Dpto. de Anal. Matem., Estad. e I.O. y Matemática Aplicada, Universidad de Málaga, Málaga, Spain

^c Área de Ingeniería Hidráulica, Universidad de Córdoba, Córdoba, Spain

ARTICLE INFO

Keywords:

Dispersive waves
Non-hydrostatic models
Weighted average
Depth-integrated modeling
Finite volume
Finite difference

ABSTRACT

Efficient modeling of flow physics is a prerequisite for a reliable computation of free-surface environmental flows. Non-hydrostatic flows are often present in shallow water environments, making the task challenging. In this work, we use the method of weighted residuals for modeling non-hydrostatic free surface flows in a depth-averaged framework. In particular, we focus on the Vertically Averaged and Moment (VAM) equations model. First, a new derivation of the model is presented using expansions of the field variables in sigma-coordinates with Legendre polynomials basis. Second, an efficient two-step numerical scheme is proposed: the first step corresponds to solving the hyperbolic part with a second-order path-conservative PVM scheme. Then, in a second step, non-hydrostatic terms are corrected by solving a linear Poisson-like system using an iterative method, thereby resulting in an accurate and efficient algorithm. The computational effort is similar to the one required for the well-known Serre-Green-Naghdi (SGN) system, while the results are largely improved. Finally, the physical aspects of the model are compared to the SGN system and a multilayer model, demonstrating that VAM is comparable in physical accuracy to a two-layer model.

1. Introduction

The computation of free-surface water flows in environmental hydraulics entails accurate and efficient modeling of important physical phenomena, including flows over obstacles, tsunami propagation, and run-up and dam break waves. The horizontal length scales in the shallow water framework are generally more significant than the vertical ones. The dispersionless nonlinear shallow water equations (SWE), derived by assuming vertical hydrostatic pressure distribution and depth-independent horizontal velocity, are often a reasonable choice.

However, the hydrostatic pressure hypothesis is no longer valid in many applications, such as the propagation of undular bores in an estuary or in the dispersive waves propagating over an obstacle. Vertical acceleration is significant in these flows, and a significant dynamic component influences the pressure distribution. Therefore, for a correct simulation of these types of flows, it becomes necessary to explore other models that consider non-hydrostatic effects.

* Corresponding author.

E-mail address: escalante@uma.es (C. Escalante).

<https://doi.org/10.1016/j.jcp.2024.112882>

Received 2 December 2022; Received in revised form 2 November 2023; Accepted 21 February 2024

Available online 27 February 2024

0021-9991/© 2024 The Author(s). Published by Elsevier Inc. This is an open access article under the CC BY-NC-ND license (<http://creativecommons.org/licenses/by-nc-nd/4.0/>).

The full three-dimensional (3D) flow modeling is still costly from the computational point of view, especially for large-scale domains and long-time simulations. Therefore, alternative modeling approaches that balance computational cost and physical accuracy are considered by vertically averaging the 3D equations. The vertically-averaged modeling of non-hydrostatic flows has been accomplished traditionally by resorting to two leading families of models: (i) Boussinesq-type models and (ii) depth-averaged non-hydrostatic models.

Boussinesq-type models account for the non-hydrostaticity of flow by retaining high-order terms in the Taylor expansion of the velocity potential in the momentum equations. For instance, this is the approach used in [1,9,57,40,51,54,67,47,45,58], among others. This approach allows for an accurate characterization of the dispersive effects from shallow to intermediate water depths. However, the velocity-dependent extra-terms retained in the governing equations contain high-order derivatives, which results in complex systems that often require careful numerical discretization.

Contrary to Boussinesq type models, depth-averaged non-hydrostatic models use first-order derivatives, incorporating dispersive effects by retaining some vertical effects in the depth-averaging process for SWE. More explicitly, the vertical velocity or non-hydrostatic pressure is not assumed to be negligible, and the pressure is split into a hydrostatic and a non-hydrostatic part. The simplest choice of non-hydrostatic model considers a vertical 1-layer division, where the horizontal velocity is assumed constant (see, for instance, [68,10,24]). The dispersive properties of non-hydrostatic models can be improved by considering multilayer models, where the vertical domain is decomposed into a prescribed number of layers. Within these layers, the velocity and pressure variables are averaged in the vertical direction. In [63], 1-layer and 2-layer models are presented using a finite-difference algorithm. The two-layer version of the model is presented in [6] or [25]. Moreover, multilayer non-hydrostatic models are found in [30].

As it was shown in [23], there is a straight relation between Boussinesq and non-hydrostatic models. Most well-known Boussinesq models may be written in an equivalent non-hydrostatic formulation. Moreover, writing them as non-hydrostatic pressure systems avoids using high-order derivatives that are not easy to treat numerically.

In recent years, several alternatives to deal with non-hydrostatic flow modeling were proposed. In [2–4], a semi-integrated approach was proposed by which depth-averaged quantities are determined by accounting for the 3D solution of the vorticity field, thus removing the need of the irrotational flow assumption and allowing for an inherent modeling of dissipative mechanism due to wave breaking. Another possible method to model non-hydrostatic free surface flows is the method of weighted residuals. This technique was originally proposed by Green and Naghdi [40,39,38,41,42], although it has not been properly acknowledged in the literature. They developed the theory of a Cosserat surface or the theory of “directed fluid sheet”, wherein the mass and momentum conservation laws, the velocity vector is expanded in terms of some basis functions depending on the vertical coordinate. The expansions contain proportionality coefficients multiplying the basis functions to be determined as part of the solution. Given that the 3D flow equations cannot satisfy these expansions in an arbitrary point of the flow, Green and Naghdi proposed to seek solutions satisfied “at large”, e.g., forming integral statements where the residuals of each conservation law are multiplied by a test function. Green and Naghdi’s theory is, therefore, a variational method where the dependence of a system of 3D equations on the vertical coordinate is removed. In the usual case, the test functions are taken equal to the basis functions, resulting in a Galerkin procedure. The lowest-order version of their theory is the so-called Serre-Green-Naghdi theory [59], which does not require the use of variational statements using test functions different from unity [18]. Interestingly, the method is not originally from Green and Naghdi but originates from the charming work of Kantorovich and Krylov [44]. They presented in their book exactly the procedure described above with application to the solution of the Poisson equation. The method of Kantorovich and Krylov [44], or the Green-Naghdi theory [40,39] is thus a Galerkin procedure suitable to produce vertically-averaged systems of conservation laws for non-hydrostatic flows. The Serre-Green-Naghdi equations constitute a handy tool for water wave modeling, and accurate results can be found in the literature (see [5,21,29,46,52,49,53,56]). The high-level version of Green-Naghdi theory was developed in [22,73,74], among others. They developed an efficient finite-difference scheme and demonstrated the increased accuracy of the high-level Green-Naghdi theory when the level of the theory is progressively increased. In [70,69], a similar method was proposed, where the variational statements were used only in the horizontal projection of the momentum equation.

The weighted residual method was used in open-channel flow applications by Steffler and Jin [62], who proposed the Vertically Averaged and Moment (VAM) equations model. However, it was not stated that the method is an application of Green-Naghdi theory. In fact, it can be demonstrated that the basis functions used by Steffler and Jin [62] are the first two shifted Legendre polynomials. In contrast, for the test functions, they took moments of the residuals with respect to the centroid of the flow section; thus, the name “Moment” equations they used for the integrals of the weighted residuals. However, taking moments produces identical statements using the first shifted Legendre polynomial as a test function. Therefore, the VAM model is a particular application of Green-Naghdi theory obtained with a Galerkin procedure using Cartesian coordinates and an orthogonal base formed with shifted Legendre polynomials, as is demonstrated in this work. The model was applied in [35,34,36] to steady river flows and in [12,14] to unsteady flows in the river and maritime environment. The only phase-resolving model to solve this formidable set of nonlinear PDEs is the finite-volume finite-difference scheme devised in [12]. Moreover, in [32], a MATLAB software platform was presented for modeling the VAM model.

Finally, highly accurate approaches in a potential flow framework include the Coupled Mode System (CMS) in [8,55], and a spectral approach in the vertical with Chebyshev polynomials shown in [71,72].

To the best of the authors’ knowledge, there is not a systematic derivation of the VAM method, the computational efficiency and mathematical stability have not been targeted nor studied, and its physical features are not systematically compared with other approaches. Numerical aspects are crucial for accurately reproducing the physical phenomena by computation. Furthermore, studying the accuracy and efficiency of the weighted residual models versus other models would be interesting. This comparison is interesting from a physical standpoint and a practical point of view. The objectives of this work are elaborated in the three main

steps as follows: (i) First, a new derivation of the VAM model is presented using sigma-coordinates and a Galerkin procedure, thereby resulting in a generalized procedure; (ii) an accurate, robust and efficient numerical approach for VAM model is proposed, (iii) the physical accuracy of the VAM model predicting dispersive effects against other non-hydrostatic models is systematically investigated.

The paper is organized as follows: Section 2 states the VAM governing equations while their derivation process is described. Although the model is not new, the derivation and the formulation presented in this work differ from the original. The alternative VAM formulation permits us to later develop and propose in Section 3 an efficient numerical scheme based on a two-step approach: (i) the hyperbolic part is firstly solved using a second-order path-conservative PVM scheme, and (ii) the hydrostatic terms are then corrected by solving a linear Poisson-like system using an iterative scheme. Later, in Section 4, the numerical method for the VAM model is applied to several test cases as compared with experimental data and the performance of the previous existing numerical scheme for the VAM model [12], which relies on a hybrid FV-FD scheme along with a time evolution Newton-Raphson (NR) iterative scheme. The results are compared with other models, including the SGN equations and the two-layer non-hydrostatic model. Finally, conclusions of this study are drawn.

2. Description of the model

For the sake of simplicity, we consider here a two-dimensional flow over an uneven fixed bed, although everything might be generalized to the 3D case. Let (x, z) be the horizontal and vertical directions, respectively, and (u, w) the velocity vector. The incompressible Navier-Stokes system for a fluid with constant density is given by

$$\begin{cases} \partial_x u + \partial_z w = 0, \\ \partial_t u + u \partial_x u + w \partial_z u + \partial_x p_T = \partial_x \sigma_{xx} + \partial_z \sigma_{xz}, \\ \partial_t w + u \partial_x w + w \partial_z w + \partial_z p_T = -g + \partial_x \sigma_{zx} + \partial_z \sigma_{zz}. \end{cases} \quad (1)$$

Where $\sigma = \mu(\nabla(u, w) + \nabla(u, w)^T)$ is the deviatoric tensor (whose components are denoted $\sigma_{xx}, \sigma_{xz}, \sigma_{zx}, \sigma_{zz}$) and μ is the viscosity coefficient. Following [33], we shall only retain the viscous coefficient $\sigma_{xz} = \sigma_{zx} = \partial_z u + \partial_x w$. Moreover, we assume that

$$\sigma_{xz}|_{z=\eta} = 0, \quad \sigma_{xz}|_{z=b} = \tau, \quad (2)$$

where τ is a friction term that will be described later.

We shall consider a decomposition of the pressure into hydrostatic and non-hydrostatic components:

$$p_T = p_H + p, \quad \text{with} \quad \partial_z p_H = -g.$$

We denote by $h(t, x)$ the fluid depth and define $b(x)$ the bottom topography. We shall denote by $\eta(t, x) = h(t, x) + b(x)$ the free surface. As boundary conditions, we take the usual kinematic conditions at the bottom ($z = b$) and free surface ($z = \eta$):

$$u|_{z=b} \partial_x b = w|_{z=b}, \quad \partial_t \eta + u|_{z=\eta} \partial_x \eta = w|_{z=\eta}.$$

We write system (1) in the so-called σ -coordinates. To this end, we consider the change of variable given by

$$\xi = \frac{z-b}{h}, \quad \text{where } \xi \in [0, 1] \text{ for } z \in [b, \eta].$$

Notice that $\xi = 0$ (respectively $\xi = 1$) corresponds to the bottom $z = b$ (respectively free surface $z = \eta$) level (see Fig. 1). Then, denoting by $\tilde{\psi}(t, x, \xi) = \psi(t, x, \xi h + b)$, the differential operators read

$$\partial_\xi \tilde{\psi} = h \partial_z \psi$$

and

$$h \partial_s \psi = \partial_s (h \tilde{\psi}) - \partial_\xi (\xi h + b) \tilde{\psi}, \quad \text{for } s \in \{t, x\}.$$

Taking into account the new variables, the pressure is written as

$$\tilde{p} = \tilde{p}_H + \tilde{p}, \quad \text{with} \quad \partial_\xi \tilde{p}_H = -gh,$$

where it is clear that assuming that the pressure is null at the surface, we obtain the expression for the hydrostatic pressure

$$\tilde{p}_H = -gh(\xi - 1).$$

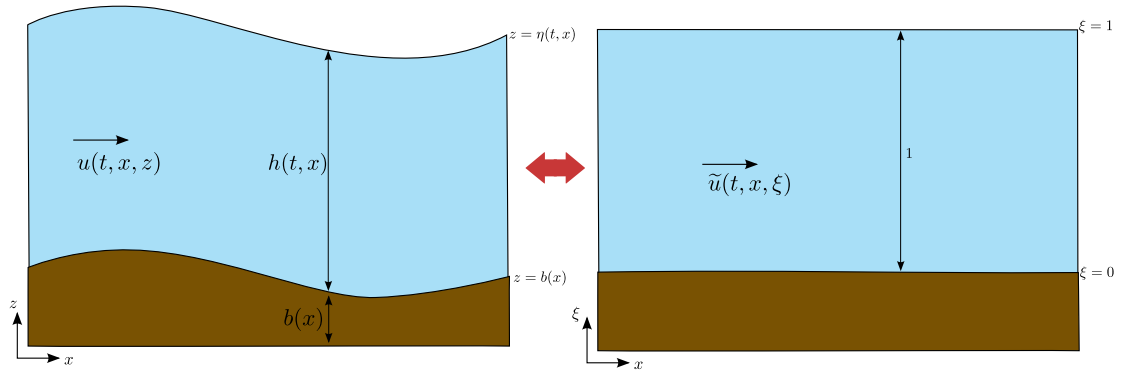


Fig. 1. Sketch of the definition of 2D free surface flow and σ -coordinate transformation.

Then system (1) in σ -coordinates reads

$$\begin{cases} \partial_x (h\tilde{u}) + \partial_\xi (\tilde{w} - \tilde{u}\partial_x(\xi h + b)) = 0, \\ \partial_t (h\tilde{u}) + \partial_x (h\tilde{u}^2 + h\tilde{p}) + gh\partial_x(b + h) \\ \quad + \partial_\xi (\omega\tilde{u} - \tilde{p}\partial_x(h\xi + b)) = \partial_\xi \tilde{\sigma}_{xz}, \\ \partial_t (h\tilde{w}) + \partial_x (h\tilde{u}\tilde{w}) + \partial_\xi (\omega\tilde{w} + \tilde{p}) = \partial_x (h\tilde{\sigma}_{zx}) - \partial_\xi (\partial_x(\xi h + b)\tilde{\sigma}_{zx}), \end{cases} \quad (3)$$

where ω is given by

$$\omega(t, x, \xi) = \tilde{w}(\xi) - (\partial_t(h\xi + b) + \tilde{u}(\xi)\partial_x(h\xi + b)).$$

Boundary conditions are then given by

$$\begin{aligned} \omega|_{\xi=0} &= \tilde{u}|_{\xi=0} \partial_x b - \tilde{w}|_{\xi=0} = 0, \\ \omega|_{\xi=1} &= \partial_t \eta + \tilde{u}|_{\xi=1} \partial_x \eta - \tilde{w}|_{\xi=1} = 0. \end{aligned}$$

For simplicity, we drop the symbol $\tilde{(\cdot)}$.

Consider now an orthogonal basis of $\mathbb{P}_N[\xi]$ in the interval $[0, 1]$, consisting of the Legendre polynomials

$$\phi_j : [0, 1] \rightarrow \mathbb{R}, \quad j = 0, 1, \dots, N.$$

In particular, in this paper, we set by choice $N = 2$, and the Legendre basis is reduced to

$$\phi_0(\xi) = 1, \quad \phi_1(\xi) = 1 - 2\xi, \quad \phi_2(\xi) = 1 - 6\xi + 6\xi^2.$$

Notice that these polynomials satisfy

$$\phi_i(0) = 1, \quad \text{and} \quad \int_0^1 \phi_i(\xi) \phi_j(\xi) d\xi = \mu_i \delta_{ij},$$

where δ_{ij} is the Kronecker symbol and μ_i is the square norm of ϕ_i in $\mathbb{P}_N[\xi]$.

The VAM model introduced in [12] considers an approximation $u \in \mathbb{P}_1[\xi]$, $w, p \in \mathbb{P}_2[\xi]$, which will be written in the Legendre polynomial basis as

$$u = u_0\phi_0 + u_1\phi_1, \quad w = w_0\phi_0 + w_1\phi_1 + w_2\phi_2, \quad p = p_0\phi_0 + p_1\phi_1 + p_2\phi_2.$$

We shall write as well

$$\sigma_{xz} = \sigma_0\phi_0 + \sigma_1\phi_1 + \sigma_2\phi_2.$$

Nevertheless, remark that the coefficients σ_j can be expressed in terms of the coefficients u_j and w_j .

In [12], a linear vertical distribution for turbulent shear stresses was assumed, meaning $\sigma_2 \approx 0$. Doing this hypothesis, from (2) we get

$$\sigma_0 = \sigma_1 = \frac{1}{2} \tau.$$

Since the basis is orthogonal, it results

$$\int_0^1 f(t, x, z) \phi_j(\xi) d\xi = \mu_j f_j(t, x), \quad \text{for } f \in \{u, w, p\} \text{ and } j = 0, 1, 2,$$

where we are setting $u_2 = 0$.

Multiplying system (3) by ϕ_j for $j = 0, 1$ and integrating in the vertical direction interval $[0, 1]$ gives

$$\left\{ \begin{array}{l} \partial_t h + \partial_x(hu_0) = 0, \\ \partial_t(hu_0) + \partial_x \left(hu_0^2 + \frac{1}{3} hu_1^3 + hp_0 \right) + gh\partial_x \eta = -2p_1 \partial_x b - \tau, \\ \partial_t(hw_0) + \partial_x \left(hu_0 w_0 + \frac{1}{3} hu_1 w_1 \right) = 2p_1 + \partial_x(h\sigma_0) + \tau \partial_x b, \\ h\partial_x u_0 + \frac{1}{3} \partial_x(hu_1) + \frac{1}{3} u_1 \partial_x h + 2(w_0 - u_0 \partial_x b) = 0, \\ \frac{1}{3} \partial_t(hu_1) + \frac{1}{3} \partial_x(2hu_0 u_1 + hp_1) - \frac{1}{3} u_0 \partial_x(hu_1) - \left(p_0 - \frac{1}{3} p_1\right) \partial_x h - 2(p_0 - p_1) \partial_x b = 2\sigma_0 - \tau, \\ \frac{1}{3} \partial_t(hw_1) + \frac{1}{3} \partial_x(hu_0 w_1) + \frac{1}{3} \partial_x \left(u_1 \left(hw_0 + \frac{2}{5} hw_2 \right) \right) + \frac{1}{3} \left(\frac{1}{5} w_2 - w_0 \right) \partial_x(hu_1) + 2p_0 - p_b \\ \quad = \frac{1}{3} \partial_x(h\sigma_1) + \frac{1}{3} \sigma_1 \partial_x h - 2\sigma_0 \partial_x(h/2 + b) - \tau \partial_x b, \end{array} \right.$$

where p_b is the non-hydrostatic pressure at the bottom, given by $p_b = p_0 + p_1 + p_2$. The previous system, consisting of 6 equations for 9 variables, is completed with the assumption that the non-hydrostatic pressure vanishes at the surface $p_0 - p_1 + p_2 = 0$ and the corresponding kinematic conditions

$$\partial_t \eta + u|_{\xi=1} \partial_x \eta - w|_{\xi=1} = 0,$$

$$u|_{\xi=0} \partial_x b - w|_{\xi=0} = 0.$$

Given the choice of the Legendre basis, we have

$$u|_{\xi=0} = u_0 + u_1, \quad u|_{\xi=1} = u_0 - u_1, \quad w|_{\xi=0} = w_0 + w_1 + w_2, \quad w|_{\xi=1} = w_0 - w_1 + w_2,$$

that used in the kinematic conditions equations gives

$$\partial_t \eta + (u_0 - u_1) \partial_x \eta = w_0 - w_1 + w_2,$$

$$(u_0 + u_1) \partial_x b = w_0 + w_1 + w_2.$$

Subtracting and adding both equations, we write them in the following equivalent way:

$$h\partial_x u_0 + u_1 \partial_x h + 2(u_1 \partial_x b - w_1) = 0,$$

$$h\partial_x u_0 + u_1 \partial_x h + 2(w_0 + w_2 - u_0 \partial_x b) = 0.$$

Remark 1. A closure relation is needed for the friction term τ . Following [11,33], the friction term could be approached as

$$\tau = \epsilon |\tilde{u}_{\xi=l/h}| \tilde{u}_{\xi=l/h},$$

where $\tilde{u}_{\xi=l/h}$ is the water velocity at a distance l near the bed. In practice, $l \ll h$ and here we shall identify $\tilde{u}_{\xi=l/h}$ with the velocity at the bottom $u_0 + u_1$, which gives

$$\tau = \epsilon |u_0 + u_1| (u_0 + u_1).$$

Moreover, following [11,33], friction law may be related to the classical Gauckler-Manning friction formula.

2.1. Compact form and hyperbolicity of the underlying hydrostatic system

The VAM model, as introduced here, can be written as the system

$$\begin{cases} \partial_t h + \partial_x(hu_0) = 0, \\ \partial_t(hu_0) + \partial_x\left(hu_0^2 + \frac{1}{3}hu_1^2 + hp_0\right) + gh\partial_x\eta = -2p_1\partial_x b - \tau, \\ \partial_t(hw_0) + \partial_x\left(hu_0w_0 + \frac{1}{3}hu_1w_1\right) = 2p_1 + \frac{1}{2}\partial_x(h\tau) + \tau\partial_x b, \\ \partial_t(hu_1) + \partial_x(2hu_0u_1 + hp_1) - u_0\partial_x(hu_1) - (3p_0 - p_1)\partial_x h - 6(p_0 - p_1)\partial_x b = 0, \\ \partial_t(hw_1) + \partial_x\left(hu_0w_1 + u_1\left(hw_0 + \frac{2}{5}hw_2\right)\right) + \left(\frac{1}{5}w_2 - w_0\right)\partial_x(hu_1) + 6(p_0 - p_1) \\ = \frac{1}{6}\partial_x(h\tau) + \frac{1}{6}\tau\partial_x h - \tau\left(\frac{h}{2} + \partial_x b\right), \end{cases} \quad (4)$$

together with the constraints

$$\begin{cases} h\partial_x u_0 + \frac{1}{3}\partial_x(hu_1) + \frac{1}{3}u_1\partial_x h + 2(w_0 - u_0\partial_x b) = 0, \\ h\partial_x u_0 + u_1\partial_x h + 2(u_1\partial_x b - w_1) = 0, \\ h\partial_x u_0 + u_1\partial_x h + 2(w_0 + w_2 - u_0\partial_x b) = 0 \end{cases} \quad (5)$$

We write (4)-(5) in a more compact form:

$$\begin{cases} \partial_t U + \partial_x F(U, w_2) + G(U, w_2)\partial_x U + S(U)\partial_x b + \mathcal{T}(U, \partial_x U, P, \partial_x P, \partial_x b) = S_{fric}(U), \\ \mathcal{I}_1(U, \partial_x U, \partial_x b) = 0, \\ \mathcal{I}_2(U, \partial_x U, \partial_x b) = 0, \\ w_2 = -(w_0 + w_1) + (u_0 + u_1)\partial_x b, \end{cases} \quad (6)$$

with

$$U = \begin{pmatrix} h \\ hu_0 \\ hu_1 \\ hw_0 \\ hw_1 \end{pmatrix}, \quad P = \begin{pmatrix} hp_0 \\ hp_1 \end{pmatrix}, \quad F(U, w_2) = \begin{pmatrix} hu_0 \\ hu_0^2 + \frac{1}{3}hu_1^2 \\ hu_0w_0 + \frac{1}{3}hu_1w_1 \\ 2hu_0u_1 \\ hu_0w_1 + u_1\left(hw_0 + \frac{2}{5}hw_2\right) \end{pmatrix},$$

$$G(U, w_2) = ghE_{2,1} - u_0E_{4,3} - \left(\frac{1}{5}w_2 - w_0\right)E_{5,3}, \quad S(U) = ghe_2,$$

where $E_{i,j}$ represents the usual elements of the canonical basis for matrices of size 5×5 , and e_2 is the second element of the canonical basis in \mathbb{R}^5 , that is,

$$G(U, w_2)\partial_x U = \begin{pmatrix} 0 \\ gh\partial_x h \\ 0 \\ -u_0\partial_x(hu_1) \\ -\left(\frac{1}{5}w_2 - w_0\right)\partial_x(hu_1) \\ 0 \end{pmatrix}, \quad S(U)\partial_x b = \begin{pmatrix} 0 \\ gh\partial_x b \\ 0 \\ 0 \\ 0 \end{pmatrix}.$$

The friction terms are given by

$$S_{fric}(U) = \begin{pmatrix} 0 \\ -\tau \\ 0 \\ \frac{1}{2}\partial_x(h\tau) + \tau\partial_x b \\ \frac{1}{6}\partial_x(h\tau) + \frac{1}{6}\tau\partial_x h - \tau(\frac{h}{2} + \partial_x b) \end{pmatrix}.$$

The non-hydrostatic terms correspond to

$$\mathcal{T}(U, \partial_x U, P, \partial_x P, \partial_x b) = \begin{pmatrix} 0 \\ \partial_x(hp_0) + 2p_1\partial_x b \\ -2p_1 \\ \partial_x(hp_1) - (3p_0 - p_1)\partial_x h - 6(p_0 - p_1)\partial_x b \\ 6(p_0 - p_1) \end{pmatrix},$$

and the constraints

$$\mathcal{I}_1(U, \partial_x U, \partial_x b) = h\partial_x u_0 + \frac{1}{3}\partial_x(hu_1) + \frac{1}{3}u_1\partial_x h + 2(w_0 - u_0\partial_x b),$$

$$\mathcal{I}_2(U, \partial_x U, \partial_x b) = h\partial_x u_0 + u_1\partial_x h + 2(u_1\partial_x b - w_1).$$

Now, let us consider the underlying hydrostatic pressure system given by

$$\partial_t U + \partial_x F(U, w_2) + G(U)\partial_x U + S(U)\partial_x b = 0. \quad (7)$$

It can be easily checked that (7) can be written in a quasi-linear form as

$$\partial_t \begin{pmatrix} U \\ b \end{pmatrix} + \left(\frac{A(U, w_2)}{0} \middle| \frac{S(U)}{0} \right) + \partial_x \begin{pmatrix} U \\ b \end{pmatrix} = 0$$

with

$$A(U, w_2) = J_F + G(U, w_2),$$

where J_F is the Jacobian of the flux F with respect to the conserved variables U . The eigenvalues of the matrix $A(U, w_2)$ are

$$\lambda_1 = u_0, \quad \lambda_{2,3} = u_0 \pm \frac{1}{\sqrt{3}}u_1, \quad \lambda_{4,5} = u_0 \pm \sqrt{gh + u_1^2}, \quad \lambda_6 = 0,$$

and therefore, the system is hyperbolic, and the full eigenstructure can be explicitly computed.

2.2. Link with existing dispersive systems in the literature

As presented here, the VAM model differs from the one presented in [12]. Indeed, in that paper, the original variables in (1) were assumed to have the following polynomial approximations

$$u(t, x, z) = \hat{u}_0(t, x) - \hat{u}_1(t, x)(1 - 2\xi),$$

$$w(t, x, z) = w_b(t, x)(1 - \xi) + 4\hat{w}_2(t, x)\xi(1 - \xi) + w_\eta(t, x)\xi,$$

$$p(t, x, z) = \hat{p}_1(t, x)(1 - \xi) + 4\hat{p}_2(t, x)\xi(1 - \xi),$$

where w_b and w_η are the vertical velocities at the bottom and the surface, respectively, and $\xi = (z - b)/h$. It is then clear that the following relations hold:

$$w_b = w_0 + w_1 + w_2, \quad w_\eta = w_0 - w_1 + w_2, \quad \hat{u}_0 = u_0, \quad \hat{u}_1 = -u_1, \quad \hat{p}_1 = p|_{z=b} = p_0 + p_1 + p_2,$$

and integrating w and p in the vertical direction

$$\frac{1}{3}\hat{w}_2 = \frac{w_b + w_\eta}{2} - w_0, \quad \frac{1}{3}\hat{p}_2 = \hat{p}_1 - p_0 = p_1 + p_2.$$

Then, the first three equations in [12] are obtained by integrating (1) in the vertical direction, that is, considering

$$\bar{f}(t, x) = \frac{1}{h} \int_b^\eta f(t, x, z) dz = \int_0^1 \tilde{f}(t, x, \xi) d\xi = f_0(t, x),$$

for any variable f , the first three equations coincide.

Then, the other three equations are obtained by considering the weighted residuals, this is, the equations are multiplied by

$$\frac{1}{h} \int_b^\eta 2 \left(\frac{z-b}{h} - \frac{1}{2} f(t, x, z) \right) dz = \int_0^1 (2\xi - 1) \tilde{f}(t, x, \xi) d\xi = \int_0^1 \phi_1(\xi) \tilde{f}(t, x, \xi) d\xi,$$

so that the other three equations also coincide, although they are written using the unknowns \hat{f} for each variable f .

In [27], a new family of non-hydrostatic layer-averaged models was presented that are closely related to the VAM system. They were described using the multi-layer approach and a similar averaging process as in [12]. In particular, one can find the LIN-NH₂ which is comparable to the VAM system, the difference being that the pressure is assumed to be $\mathbb{P}_3[\xi]$ instead of $\mathbb{P}_2[\xi]$. That allows to prove a dissipative energy balance for that particular model.

2.3. Dispersive properties of linear waves

In this Subsection, the dispersive features of the model are presented for a complete description of the VAM model. In particular, we focus on the linear dispersion relation for the wave and group velocities and the linear shoaling gradient.

As usual, the governing equations are linearized around the steady-state solution corresponding to a constant water thickness H and zero velocity given by

$$b = -H, \quad u_0 = u_1 = w_0 = w_1 = 0,$$

where we are considering the perturbations of free surface η with respect to the zero level. We then consider the following asymptotic expansion

$$h = H + \epsilon \eta^{(1)} + \mathcal{O}(\epsilon^2), \quad f = \epsilon f^{(1)} + \mathcal{O}(\epsilon^2), \quad \forall f \in \{u_0, u_1, w_0, w_1\}.$$

In the following, we omit the notation ⁽¹⁾ for the sake of simplicity. Using this linearization in (4)-(5), we shall neglect $\mathcal{O}(\epsilon^2)$ terms and keep the system at first order:

$$\left\{ \begin{array}{l} \partial_t \eta + H \partial_x u_0 = 0, \\ \partial_t u_0 + \partial_x p_0 + g \partial_x \eta = 0, \\ H \partial_t w_0 = 2p_1, \\ \partial_t u_1 + \partial_x p_1 = 0, \\ H \partial_t w_1 + 6(p_0 - p_1) = 0, \end{array} \right. \quad (8)$$

together with the restrictions

$$\left\{ \begin{array}{l} H \partial_x u_0 + \frac{H}{3} \partial_x u_1 + 2w_0 = 0, \\ H \partial_x u_0 - 2w_1 = 0, \\ H \partial_x u_0 + 2(w_0 + w_2) = 0. \end{array} \right. \quad (9)$$

We then conduct a standard Stokes-type Fourier analysis where the linearized variables are supposed to be of the form

$$f(x, t) = \bar{f} \cdot e^{i(\omega t - kx)}, \quad \forall \bar{f} \in \{\eta, u_0, u_1, w_0, w_1\},$$

where ω is the wave frequency and k the wave number. By substituting the previous expression in (8)-(9), we get a linear system for the unknowns \bar{f} . Non-trivial solutions for the aforementioned linear system are given when the following linear dispersion relation for the wave celerity, $C = \omega/k$, holds:

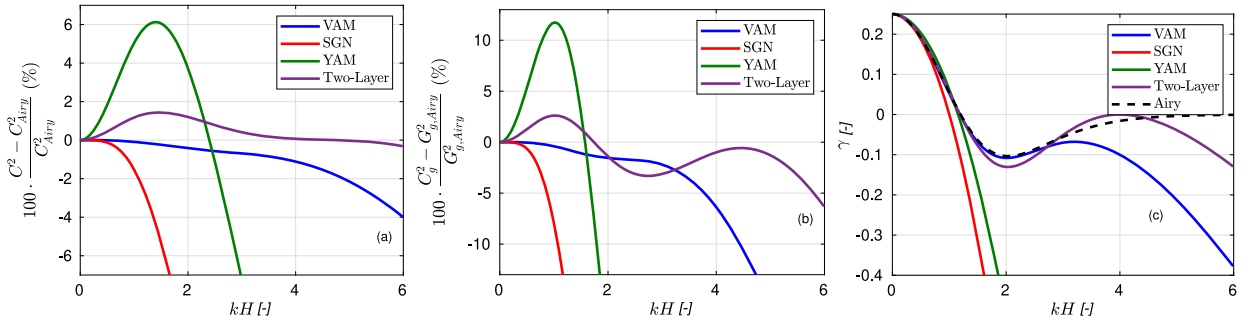


Fig. 2. (a), (b) Relative errors (in percentage) for the wave celerity C^2 and group velocity C_g^2 respectively. (c) Comparison with the shoaling gradient γ . (For interpretation of the colors in the figure(s), the reader is referred to the web version of this article.)

$$\frac{C^2}{\sqrt{gH}} = \frac{1 + \frac{(kH)^2}{12}}{1 + 5\frac{(kH)^2}{12} + \frac{(kH)^4}{144}}.$$

Then, following a general procedure similar to the one described in [27], the group velocity $C_g = C + k\partial_k C$ can be obtained from the linear dispersion relation for C , and it yields

$$\frac{C_g^2}{\sqrt{gH}} = \frac{1 + \frac{(kH)^2}{3} + \frac{(kH)^4}{12} + \frac{(kH)^6}{108} + \frac{kH^8}{1296}}{1 + \frac{4(kH)^2}{3} + \frac{31(kH)^4}{48} + \frac{233(kH)^6}{1728} + \frac{233(kH)^8}{20736} + \frac{31(kH)^{10}}{82944} + \frac{(kH)^{12}}{186624} + \frac{(kH)^{14}}{35831808}}.$$

An interesting index that measures the shoaling of impinging waves in the presence of a slope is the shoaling gradient coefficient, proposed by Madsen et al. (see [51]). The shoaling coefficient γ is defined as the quantity that fulfills the relation

$$\frac{\partial_x \eta}{\eta} = -\gamma \frac{\partial_x H}{H}.$$

As for the group velocity, we follow the general procedure for the computation of γ from the linear dispersion relation for C (see [27]), and it yields

$$\gamma = \frac{1}{4} - \frac{\frac{kH^2}{4} + \frac{kH^4}{32} + \frac{kH^6}{2304} + \frac{kH^8}{4608} + \frac{kH^{10}}{82944}}{1 + \frac{kH^2}{3} + \frac{kH^4}{12} + \frac{kH^6}{108} + \frac{kH^8}{1296}}.$$

In Fig. 2, we show comparisons of the described linear dispersion relations with respect to the Airy linear theory, which establishes

$$\frac{C_{Airy}^2}{gH} = \frac{\tanh(kH)}{kH}, \quad \frac{C_{g,Airy}^2}{gH} = \frac{(2kH + \sinh(2kH))^2}{2kH(2\sinh(2kH) + \sinh(4kH))},$$

and

$$\gamma_{Airy} = kH \tanh(kH) \frac{(1 - kH \tanh(kH))(1 - \tanh^2(kH))}{(\tanh(kH) + kH(1 - \tanh^2(kH)))^2}.$$

As it is seen in Fig. 2, the proposed VAM model ensures a minimal error of less than 5% in an extended range of $kH \in [0, 4]$ for the wave celerity and group velocity. Fig. 2 also shows a comparison with the linear dispersion relations of the SGN [40], the model by Yamazaki et al. (YAM) [68], and the Two-Layer non-hydrostatic [25,30] models. It can be seen that the relative error for wave celerity is smaller for the VAM model in the range $kH \in [0, 2.7]$. For bigger values of kH , the wave celerity of the two-layer model is slightly better than the VAM model, although they both have a relative error smaller than 2% up to $kH = 4.9$. In contrast, the YAM and SGN have larger celerity errors. Concerning group velocity, the VAM model shows an error smaller than all three models up to $kH = 3.2$, although there is a small region $kH \in [1.5, 2]$ where the Two-layer model is slightly better. Similarly, the VAM model has the best shoaling gradient approximation up to $kH = 2.7$. In order to take into account a whole range in kH , let us consider the L^1 -norm relative errors for a fixed interval $[0, (kH)_{\max}]$, that is, we define

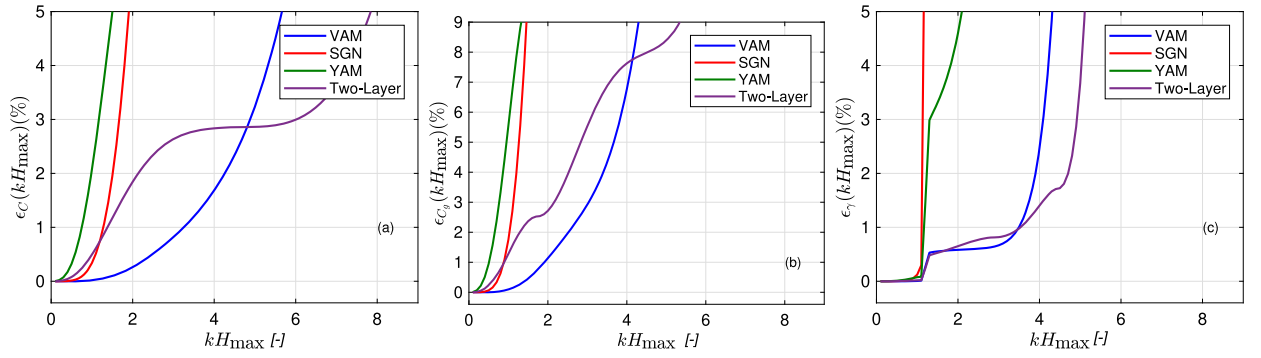


Fig. 3. (a), (b), (c) L^1 -norm errors as defined by (10) for the wave celerity C^2 , group velocity C_g^2 , and shoaling γ respectively for a given maximum wavenumber $(kH)_{\max}$.

$$\begin{aligned}
 \epsilon_C((kH)_{\max}) &= \int_0^{(kH)_{\max}} \left| \frac{C^2(kH) - C_{\text{Airy}}^2(kH)}{C_{\text{Airy}}^2(kH)} \right| dkH, \\
 \epsilon_{C_g}((kH)_{\max}) &= \int_0^{(kH)_{\max}} \left| \frac{C_g^2(kH) - C_{g,\text{Airy}}^2(kH)}{C_{g,\text{Airy}}^2(kH)} \right| dkH, \\
 \epsilon_\gamma((kH)_{\max}) &= \int_0^{(kH)_{\max}} \left| \frac{\gamma(kH) - \gamma_{\text{Airy}}(kH)}{\gamma_{\text{Airy}}(kH)} \right| dkH.
 \end{aligned} \tag{10}$$

These L^1 -norm errors, which include the cumulative error for a given interval $[0, (kH)_{\max}]$, are shown in Fig. 3 for all the systems mentioned above. Let us remark that, as an alternative method, one could consider a weighted L^1 -norm error as in [25], where a bigger weight is given for smaller values of kH . As we see in Fig. 3 when considering the whole range $kH \in [0, (kH)_{\max}]$ for the wave celerity, the VAM system performs better than the other systems up to $(kH)_{\max} = 4.8$. The same can be said for the group velocity up to $(kH)_{\max} = 4.1$ and the shoaling gradient up to $(kH)_{\max} = 3.5$. The Two-Layer system will give a better result for large ranges of wavenumbers. Nevertheless, as shown in Fig. 2, the errors rapidly increase for large values of kH .

3. Numerical scheme

Let us describe the numerical scheme used to discretize the system (6). The numerical method is based on a two-step projection-correction method. First, we shall solve the underlying non-conservative hydrostatic and hyperbolic system given by (7).

Then, in the second step, non-hydrostatic terms will be considered. System (7) is numerically approximated using a second order finite volume Polynomial Viscosity Matrix method (from now on PVM); it is a positive-preserving, well-balanced, path-conservative method based on segments [17]. As usual, we consider a set of N finite volume cells $I_i = [x_{i-1/2}, x_{i+1/2}]$ with constant lengths Δx and define

$$U_i(t) = \frac{1}{\Delta x} \int_{I_i} U(x, t) dx,$$

the cell average of the function $U(x, t)$ on cell I_i at time t . Regarding non-hydrostatic terms, we consider the mid-point x_i of each cell I_i and denote the point values of the function P at time t by

$$P_i(t) = P(x_i, t).$$

Second-order compact finite differences will approximate non-hydrostatic terms.

3.1. Time stepping

Assume given time steps Δt^n , and denote $t^n = \sum_{j \leq n} \Delta t^j$, a two-stage second-order TVD Runge-Kutta scheme [37] is adopted to obtain second-order accuracy in time. More explicitly, let us formally summarize the two stages. For a general system in the form

$$\frac{d}{dt} U(t) = \mathcal{H}(t, U(t)),$$

starting from a given approximation at time t^n , $U^{(0)} = U(t^n)$, we compute the two stages given by

$$U^{(1)} = U^{(0)} + \Delta t \mathcal{H}(t^n, U^{(0)}),$$

$$U^{(2)} = U^{(1)} + \Delta t \mathcal{H}(t^n + \Delta t, U^{(1)}).$$

Then, the approximation at time t^{n+1} is defined as

$$U^{n+1} = \frac{1}{2}U^{(0)} + \frac{1}{2}U^{(2)}.$$

In our particular case, we need to solve system (6). To do so, for each of the k th stage, $k \in \{1, 2\}$, a two-step projection-correction method is used:

- First, starting from the approximation $U^{(k-1)}$, the hyperbolic part of the system is solved by means of a second-order finite volume path-conservative PVM scheme, which is described in Section 3.2. In this way, we obtain an approximation, denoted by $U^{(\tilde{k})}$, which corresponds to the numerical solution of

$$\frac{U^{(\tilde{k})} - U^{(k-1)}}{\Delta t} + \partial_x F(U^{(k-1)}, w_2^{(k-1)}) + G(U^{(k-1)}, w_2^{(k-1)}) \partial_x U^{(k-1)} + S(U^{(k-1)}) \partial_x b = 0, \quad (11)$$

- Second, the non-hydrostatic part of the system is considered, which is solved by means of a finite difference discretization. That will lead to the solution of a Poisson-like system, which is described in Section 3.3. In this way, we obtain $U^{(k)}$ and $P^{(k)}$ as an approximation of

$$\begin{cases} \frac{U^{(k)} - U^{(\tilde{k})}}{\Delta t} + \mathcal{T}(U^{(k)}, \partial_x U^{(k)}, P^{(k)}, \partial_x P^{(k)}, \partial_x b) = 0, & (a) \\ I_1(U^{(k)}, \partial_x U^{(k)}, \partial_x b) = 0, & (b) \\ I_2(U^{(k)}, \partial_x U^{(k)}, \partial_x b) = 0, & (c) \end{cases} \quad (12)$$

Let us remark that at the end of this stage, we have to update the variable w_2 , which is done by

$$w_2^{(k)} = -(w_0^{(k)} + w_1^{(k)}) + (u_0^{(k)} + u_1^{(k)}) \partial_x b, \quad (13)$$

Remark 2. When friction is considered, it will be computed as follows:

- The fourth and fifth components of the vector $S_{fric}(U)$

$$\begin{pmatrix} 0 \\ 0 \\ 0 \\ \frac{1}{2} \partial_x (h\tau) + \tau \partial_x b \\ \frac{1}{6} \partial_x (h\tau) + \frac{1}{6} \tau \partial_x h - \tau (\frac{h}{2} + \partial_x b) \end{pmatrix}$$

are explicitly taken into account during the first step of the projection-correction method at each k th stage of the TVD Runge-Kutta method, in a similar way as the other source terms are treated.

- The second component of the vector $S_{fric}(U)$, $-\tau$, is taken into account semi-implicitly at the end of the second step of the projection-correction method at each k th stage of the TVD Runge-Kutta method as it is done in [33]. Therefore, the values $hu_0^{(k)}$ are replaced by hu_0^* as follows

$$hu_0^* = hu_0^{(k)} - \Delta t \epsilon \frac{|hu_0^{(k)} + hu_1^{(k)}|}{h^{(k)}} \frac{(hu_0^* + hu_1^{(k)})}{h^{(k)}}.$$

The usual Courant-Friedrichs-Lewy (CFL) restriction should be considered for the computation of the time step Δt .

3.2. Finite volume discretization for the underlying hyperbolic system

A second-order path-conservative PVM scheme for the discretization in space for the system (11), at the k th stage of the Runge-Kutta reads as follows (see [17,16] for further details):

$$\frac{U^{(\tilde{k})} - U^{(k-1)}}{\Delta t} = -\frac{1}{\Delta x} \left(D_{i+1/2}^{(k-1),-} + D_{i-1/2}^{(k-1),+} + \mathcal{V} I_i \right), \quad (14)$$

where, omitting the time dependence k for the sake of simplicity in the notation,

$$\begin{aligned} D_{i+1/2}^- &= D_{i+1/2}^-(U_{i+1/2}^-, U_{i+1/2}^-, w_{2,i+1/2}^-, w_{2,i+1/2}^-, b_{i+1/2}^+, b_{i+1/2}^-) \\ &= \frac{1}{2} \left(F(U_{i+1/2}^+, w_{2,i+1/2}^+) - F(U_{i+1/2}^-, w_{2,i+1/2}^-) \right. \\ &\quad \left. + G(U_{i+1/2}, w_{2,i+1/2}) (U_{i+1/2}^+ - U_{i+1/2}^-) + S(U_{i+1/2}) (b_{i+1/2}^+ - b_{i+1/2}^-) \right) \\ &\quad \pm \frac{1}{2} Q_{i+1/2} (U_{i+1/2}^+ - U_{i+1/2}^- + A_{i+1/2}^{-1} S(U_{i+1/2}) (b_{i+1/2}^+ - b_{i+1/2}^-)), \\ \mathcal{V}I_i &= F(U_{i+1/2}^-, w_{2,i+1/2}^-) - F(U_{i-1/2}^+, w_{2,i-1/2}^+) + G(U_i, w_{2,i}) (U_{i+1/2}^- - U_{i-1/2}^+) + S(U_i) (b_{i+1/2}^- - b_{i-1/2}^+) \end{aligned}$$

where

$$U_{i+1/2} = (h_{i+1/2}, (hu_0)_{i+1/2}, (hu_1)_{i+1/2}, (hw_0)_{i+1/2}, (hw_1)_{i+1/2}, b_{i+1/2})^T,$$

with

$$\begin{aligned} h_{i+1/2} &= \frac{h_{i+1/2}^+ + h_{i+1/2}^-}{2}, \quad b_{i+1/2} = \frac{b_{i+1/2}^+ + b_{i+1/2}^-}{2}, \\ (hv)_{i+1/2} &= h_{i+1/2} v_{i+1/2}, \quad v_{i+1/2} = \frac{v_{i+1/2}^+ \sqrt{h_{i+1/2}^+} + v_{i+1/2}^- \sqrt{h_{i+1/2}^-}}{\sqrt{h_{i+1/2}^+} + \sqrt{h_{i+1/2}^-}}, \quad \text{for } v = u_0, u_1, w_0, w_1, w_2. \end{aligned}$$

The values $U_{i+1/2}^\pm$ and $w_{2,i+1/2}^\pm$ are defined by a reconstruction procedure on the variables to the left ($-$) and right ($+$) of the inter-cell $x_{i+1/2}$. This reconstruction procedure uses a MUSCL reconstruction operator (see [66]) combined with a minmod limiter.

$Q_{i+1/2}$ corresponds to the viscosity matrix associated to the numerical method. In general, $Q_{i+1/2}$ is a polynomial evaluation of the Roe Matrix of the system. Here, $Q_{i+1/2}$ is defined as

$$Q_{i+1/2} = \beta_0 Id + \beta_1 A_{i+1/2},$$

being

$$\beta_0 = \frac{S_R |S_L| - S_L |S_R|}{S_R - S_L}, \quad \beta_1 = \frac{|S_R| - |S_L|}{S_R - S_L},$$

where S_L, S_R are estimates of the smallest and largest wave speeds at the interface $x_{i+1/2}$, as usual. Here, we use

$$\begin{aligned} S_L &= \min \left(u_{0,i+1/2} - \sqrt{gh_{i+1/2} + u_{1,i+1/2}^2}, u_{0,i} - \sqrt{gh_i + u_{1,i+1/2}^2} \right), \\ S_R &= \max \left(u_{0,i+1/2} + \sqrt{gh_{i+1/2} + u_{1,i+1/2}^2}, u_{0,i+1} + \sqrt{gh_{i+1} + u_{1,i+1/2}^2} \right). \end{aligned}$$

$A_{i+1/2}$ denotes the matrix

$$A_{i+1/2} = \mathcal{J}_F(U_{i+1/2}, w_{2,i+1/2}) + G(U_{i+1/2}, w_{2,i+1/2}),$$

being \mathcal{J}_F the Jacobian matrix of the flux F .

The scheme described previously corresponds to a segment path-conservative extension of the HLL scheme [43] for non-conservative systems.

3.3. Finite difference discretization for the non-hydrostatic terms

Now, we describe the discretization of the non-hydrostatic terms. For this task, we shall substitute $U^{(k)}$ from (12a) in equations (12b)-(12c), resulting in the Poisson-like equations

$$\begin{aligned} a_1 \partial_{xx} p_0^{(k)} + a_2 \partial_x p_0^{(k)} + a_3 p_0^{(k)} + a_4 \partial_{xx} p_1^{(k)} + a_5 \partial_x p_1^{(k)} + a_6 p_1^{(k)} &= RHS_1 \\ b_1 \partial_{xx} p_0^{(k)} + b_2 \partial_x p_0^{(k)} + b_3 p_0^{(k)} + b_4 \partial_{xx} p_1^{(k)} + b_5 \partial_x p_1^{(k)} + b_6 p_1^{(k)} &= RHS_2 \end{aligned} \quad (15)$$

where the coefficients a_j, b_j as well as the Right-Hand-Sides RHS_j depend on $U^{(\tilde{k})}$ and $w_2^{(\tilde{k})}$. Equations (15) are discretized using second-order finite differences. To obtain point value approximations of the non-hydrostatic pressure variables, terms $p_{0,i}^{(k)}, p_{1,i}^{(k)}$ and $RHS_{j,i}$, $j \in \{1, 2\}$, $i \in \{1, \dots, N\}$ will be approximated at every midpoint x_i of each cell I_i . Further, the corresponding space derivatives will be approximated using second-order central finite differences

$$\partial_x p_i^{(k)} = \frac{p_{i+1}^{(k)} - p_{i-1}^{(k)}}{2\Delta x}, \quad \partial_{xx} p_i^{(k)} = \frac{p_{i+1}^{(k)} - 2p_i^{(k)} + p_{i-1}^{(k)}}{\Delta x^2} \quad (16)$$

To compute the coefficients a_j , b_j , RHS_j , which contain terms depending on $U^{(\tilde{k})}$ as well as its first derivatives, we will use the averaged values on the cell I_i as second-order point value approximations at the center of the cells. Similarly, the space derivatives are computed from the averaged values using second-order finite differences

$$\partial_x U_i^{(\tilde{k})} = \frac{U_{i+1}^{(\tilde{k})} - U_{i-1}^{(\tilde{k})}}{2\Delta x}. \quad (17)$$

After replacing (16) and (17) in (15), ones obtain a linear system that is solved following an iterative method similar to the one described in [25].

Remark 3. In practice, one could use any independent linear combination of equations (12b), (12c) and (13). Nevertheless, although this is equivalent at a continuous level, it plays a relevant role at the discrete level when solving the final linear system iteratively. In practice, we have empirically found that better results are obtained when we use

$$\begin{cases} \mathcal{I}_1(U^{(k)}, \partial_x U^{(k)}, \partial_x b) + \mathcal{I}_2(U^{(k)}, \partial_x U^{(k)}, \partial_x b) = 0, \\ \mathcal{I}_1(U^{(k)}, \partial_x U^{(k)}, \partial_x b) - \mathcal{I}_2(U^{(k)}, \partial_x U^{(k)}, \partial_x b) = 0, \end{cases}$$

and then we proceed similarly as stated before. Doing so, we have found that the iterative algorithm for the linear system converges 1.6 times faster.

3.4. Final numerical scheme

For clarity, a guideline of the final numerical scheme will be highlighted as follows. For every k th stage $k \in \{1, 2\}$ of the Runge-Kutta method, the problem (6) is split into two parts. A two-step projection-correction method is used:

- Finite volume step (solving the hydrostatic system): From (14), solve explicitly the hyperbolic system at the k th stage of the Runge-Kutta:

$$\frac{U^{(\tilde{k})} - U^{(k-1)}}{\Delta t} = -\frac{1}{\Delta x} \left(D_{i+1/2}^{(k-1),-} + D_{i-1/2}^{(k-1),+} + \mathcal{V} \mathcal{I}_i \right),$$

by means of a PVM path-conservative finite volume scheme combining a MUSCL reconstruction operator to obtain the intermediate value $U^{(\tilde{k})}$ in the two-step projection-correction method that contains the numerical solution of the underlying hyperbolic system.

- Finite difference step (non-hydrostatic pressure correction):
 - Solve the Poisson-like equations (15) to obtain the non-hydrostatic pressures $P^{(k)}$. To do so, compact-centered second-order finite differences are used for the discretization of the derivatives that appear in (15), and a linear system is solved to obtain $P^{(k)}$.
 - With the computed non-hydrostatic pressure terms $P^{(k)}$, then hu_0 , hu_1 , hw_0 , hw_1 can be updated from (12a) and w_2 from (13). To do that, a second-order point value approximation in the center of the cell will be used to compute the non-hydrostatic contribution.

Finally,

$$U^{n+1} = \frac{1}{2}U^n + \frac{1}{2}U^{(2)}.$$

Remark 4. Concerning the boundary conditions and the wetting and drying treatment, we follow the procedure described in [25]. More explicitly, for the computation of values including a term in the form $\frac{1}{h}$, for very small values of the water height h , we replace

$\frac{1}{h}$ by

$$\frac{\sqrt{2}h}{\sqrt{h^4 + \max\{h^4, \varepsilon\}}},$$

for some threshold $\varepsilon > 0$. In the tests described in this paper ε is set to 10^{-6} .

4. Numerical tests

In this section, we highlight the ability of the proposed VAM numerical model to simulate a wide variety of complex situations involving dispersive water waves. Comparisons with standard numerical tests for dispersive water wave systems, including analytical

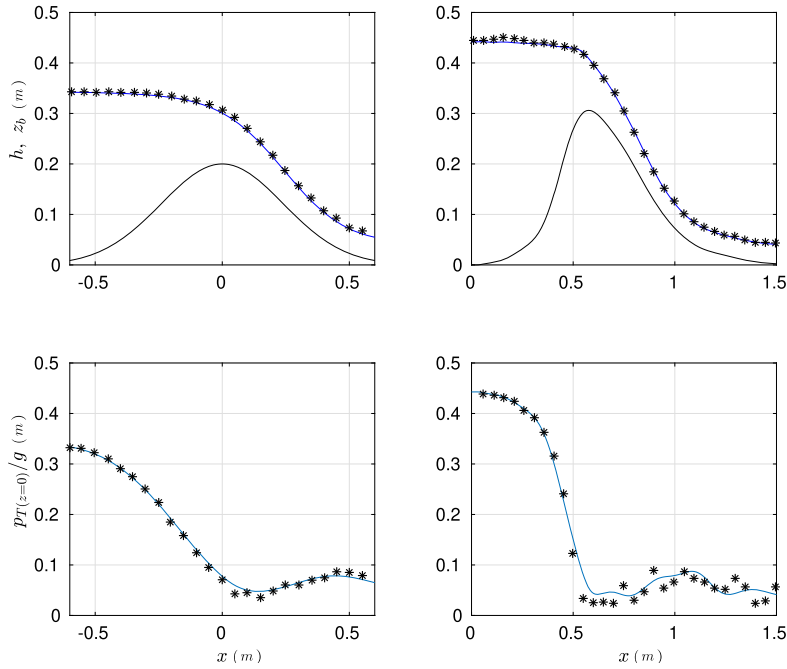


Fig. 4. Steady flow over fixed bedforms. Blue solid lines correspond to numerical results, and star symbols represent experimental data. A Gaussian profile is given on the left column, while an asymmetric profile is on the right. The upper figures represent the numerical free surface flow over the bottom (solid black line). Lower figures correspond to the bed pressure.

solutions and laboratory data, are shown. We shall also compare the results with the classic and well-known SGN introduced in [40,59,48,30].

In what follows, the gravity acceleration is set to $g = 9.81 \text{ m/s}^2$.

4.1. Steady flow over fixed bedforms

We consider a steady non-hydrostatic flow over a fixed bedform in this first test case. As the flow passes over the bottom bump, the pressure drops below the hydrostatic value due to vertical acceleration. We intend to accurately reproduce the net drag force or form drag determined by the non-hydrostatic bottom pressure distribution.

The numerical test reproduced here was experimentally investigated in [60], where symmetric and asymmetric bed forms were considered, and experimental measurements for the free-surface level and the bed pressure were obtained. A flume of length 9.15 m, width 0.3 m and 0.65 m deep was used. Constant inflow discharge was imposed. Two types of experiments are considered:

- A Gaussian profile with length 1.2 m and maximum elevation equal to 0.2 m and an inflow discharge $q = 0.11197 \text{ m}^2/\text{s}$.
- An asymmetrical hump 0.3 m high and 1.5 m long and inflow $q = 0.11165 \text{ m}^2/\text{s}$

For the first test case, we consider a computational domain given by $[-1.5, 1.5] \text{ m}$, whereas $[-0.5, 1.7] \text{ m}$ is used for the second test case. For all the test cases, the computational domain is covered with constant cells of length $\Delta x = 0.01 \text{ m}$, the CFL number is set to 0.4, and the simulation time was $t = 50 \text{ s}$.

In the first experiment, water is initially at rest to simulate the inflow, and a closed gate is located at $x = 1 \text{ m}$. The water depth is $h = 0.015 \text{ m}$, downstream of the gate and $h = 0.34 \text{ m}$ upstream. The rest of the flow variables are set initially to zero. As used in the experiment, a constant discharge boundary condition was prescribed at the upstream end of the domain, and a free-outflow boundary condition was imposed at the downstream part. The gate was removed instantaneously from the flume, generating a dam-break-like flow. In the case of the second experiment, the inflow is simulated by setting a water depth level to $h = 0.02 \text{ m}$ downstream of the gate and $h = 0.42 \text{ m}$ upstream. The friction term is neglected because the flow resistance is irrelevant in these tests.

The results are shown in Fig. 4. The numerical approach presented here for the VAM model correctly reproduces the experimental data's free surface and bed pressures.

4.2. Order of accuracy

A usual test for non-hydrostatic free-surface flows corresponds to the simulation of solitary waves. Although it is not an exact solitary wave solution for the VAM model, we consider here the general expression given in [10]:

Table 1Accuracy test. L^1 numerical errors and convergence rates for the zeroth-moment variables.

N	L^1 error h		L^1 error hu_0		L^1 error hw_0	
400	1.97e-02	0.00	5.99e-02	0.00	2.60e-02	0.00
800	6.16e-03	1.68	1.76e-02	1.77	9.14e-03	1.51
1600	1.60e-03	1.94	4.36e-03	2.01	2.46e-03	1.89
3200	3.92e-04	2.03	1.07e-03	2.03	6.02e-04	2.03

Table 2Accuracy test. L^1 numerical errors and convergence rates for the first-moment variables.

N	L^1 error hu_1		L^1 error hw_1		L^1 error hw_2	
400	2.34e-02	0.00	2.90e-02	0.00	4.35e-03	0.00
800	8.67e-03	1.43	1.09e-02	1.41	2.49e-03	0.80
1600	2.38e-03	1.87	3.03e-03	1.84	8.43e-04	1.56
3200	6.06e-04	1.97	7.61e-04	1.99	2.41e-04	1.81

$$h(t, x) = H_* + A \operatorname{sech}^2 \left(\frac{B}{H_*} (x - ct) \right), \quad u(t, x) = c \left(1 - \frac{H_*}{h(t, x)} \right), \quad (18)$$

$$w(t, x) = -\frac{cAB}{h(t, x)} \operatorname{sech}^3 \left(\frac{B}{H_*} (x - ct) \right) \sinh \left(\frac{B}{H_*} (x - ct) \right)$$

where $B = \sqrt{\frac{\gamma A}{2(A+H_*)}}$, A and H_* are constant fixed values and $c = \sqrt{g(A+H_*)}$. We denote by $\eta = h - H_*$ the corresponding free surface. The case $\gamma = 3/2$ corresponds to a solitary wave for the SGN system [59,40], which will be used throughout this paper.

Here, we set as initial condition a solitary wave using (18) with $b = H_* = 1$ m and $A = 0.1$ m. The water depth variable is initially given by h as in (18); the mean of the horizontal and vertical velocities for the VAM model, u_0 and w_0 , are given by u and w as in (18), respectively; the rest of flow variables for the VAM model are initially set to zero.

Since (18) is not an exact solution of the system, a reference solution is computed with the described second-order scheme and 51,200 cells. Free-outflow boundary conditions are imposed, and the computational domain is $[-150, 150]$ m.

The second-order scheme is run with an increasing number of cells N in the given domain, and the errors for all system variables are computed. The integration time is $T = 1$ s., and the CFL number is 0.4.

Tables 1 and 2 show the errors and the convergence rates for the conserved variables h , hu_0 , hu_1 , hw_0 , hw_1 , and hw_2 , and reveal that the theoretical order of accuracy is achieved.

4.3. Solitary wave solution

In this numerical experiment, we consider the simulation of the evolution of a large amplitude solitary wave for a large integration time. Here, we consider an initial condition given by (18) as in the previous numerical experiment with $b = H_* = 1$ m and $A = 0.55$ m.

The considered computational domain is $\Omega = [-50, 700]$ m, and it is covered with a set of constant cells of $\Delta x = 0.025$ m length. The CFL is equal to 0.4, and the final simulation time is $t = 150$ s. Free-outflow boundary conditions are imposed on both sides of the domain.

As it has been said, the solitary wave imposed as the initial condition is not an exact solitary wave solution for the VAM model. Therefore, we expected it to be perturbed and to change its shape. However, a solitary wave solution for the VAM model is reached after some time. That can be seen in Fig. 5, where amplitude increases until a stable solitary wave solution of amplitude $A = 0.65$ m is obtained. Once this stable solitary wave is reached, the wave does not increase in time. To illustrate this fact, we shall consider the energy production along the time for this test case.

Let us remark that the VAM model considered here is closely related to the LIN-NH₂ model introduced in [27]. The main difference is that the former assumes a pressure with a quadratic vertical profile while the latter uses a cubic polynomial. This distinction is important to obtain a dissipative energy balance. In [27], it is shown that LIN-NH₂ satisfies an energy dissipation equation. Nevertheless, up to our knowledge, there is no energy dissipation for VAM. However, one could measure numerically the energy of the system by considering the depth-averaged energy equation of the Euler system

$$E(x, t) = \int_0^1 \left(\frac{u^2 + w^2}{2} + g(z_b + \xi h) \right) h d\xi = \frac{h}{2} \left(u_0^2 + \frac{1}{3} u_1^2 + u_0^2 + \frac{1}{3} w_1^2 + \frac{1}{5} w_2^2 + g(\eta + z_b) \right),$$

Fig. 6 shows the time evolution of the averaged energy along the computational domain, that is

$$\bar{E}(t) = \int_{\Omega} E(x, t) dx.$$

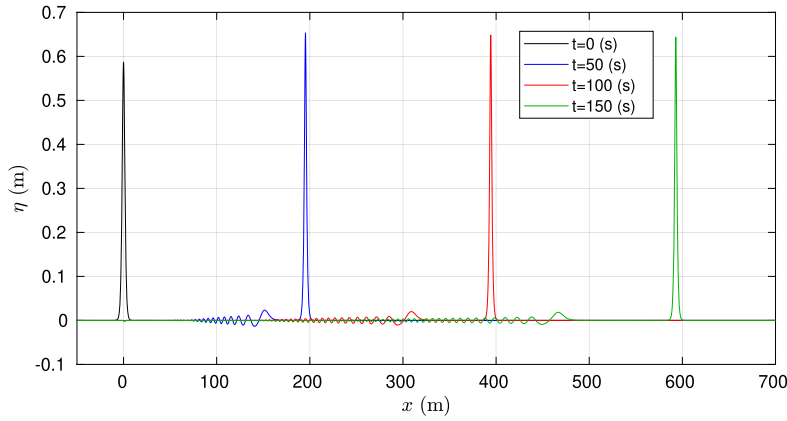


Fig. 5. Solitary wave propagation test for times: $t = 0$ s (black), $t = 50$ s (blue), $t = 100$ s (red), and $t = 150$ s (green).

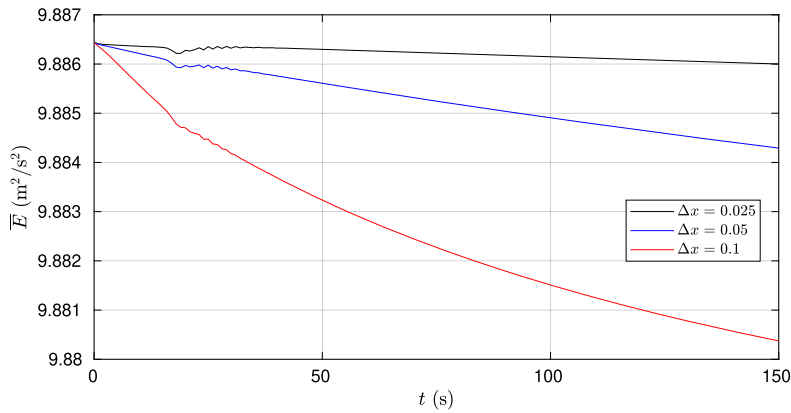


Fig. 6. Time evolution of the averaged energy along the computational domain.

As it can be stated, the energy remains bounded. In fact, one generally observes a decrease in the energy due to the numerical diffusion, as it is stated when the mesh is refined. Nevertheless, recall that the numerical scheme is not entropy satisfying, nor does the VAM system satisfy an entropy dissipation equation, so the energy is not globally decreasing.

Finally, we compare in Fig. 7 the profiles given by the computed solitary wave obtained with the VAM model; the analytical solution (18); and the solitary wave profile obtained by Tanaka solving the exact boundary value problem [64], taken from [15]. A good fitting of the solitary wave given by the VAM model with the Tanaka solution can be observed.

4.4. Solitary wave run-up on a plane beach

A classic test for non-hydrostatic shallow flows corresponds to the experimental setup by Titov and Synolakis and is described in [65]. Incident solitary waves of multiple relative amplitudes were simulated to study propagation, breaking, and run-up over a planar beach with a slope of 1 : 19.85. Experimental data are available in [65] for surface elevation at different times.

The still water level in the test case used here is $H_* = 1$ m. The bathymetry of the problem is given in Fig. 8. The initial condition for the VAM model is provided by a solitary wave of amplitude $A = 0.3$ m centered at point $x = 25$ m, and that is done using (18) as in the previous Subsection.

In this case, a friction coefficient of $\epsilon = 0.01 \text{ s} \cdot \text{m}^{-1/3}$ was used to account for the glass surface roughness effects appearing in the experiments. The computational domain $[-15, 50]$ m is covered with cells of constant length $\Delta x = 0.1$ m. The CFL number is set to 0.4, and free-outflow boundary conditions were imposed everywhere. The simulation time is $t = 15$ s.

Fig. 9 shows snapshots at different times, $t\sqrt{g/H_*} = t_0$. A good agreement between experimental and simulated data is seen. We remark that wave breaking is observed at $t\sqrt{g/H} = 20$ and 25 during the experiment. The VAM model well reproduces that wave-breaking effect without any special treatment. Moreover, the run-up agrees with the data, and the numerical scheme correctly treats the wet-dry transitions.

Now that we have concluded that the VAM system correctly reproduces the experimental data, let us compare the results of the VAM system with the ones obtained using the well-known SGN system. The comparative results are shown in Fig. 10. We remark that initially, both systems give similar results. Nevertheless, they begin to differ as time evolves and the wavefront travels up the plane beach. First, the shock front position is misplaced, and SGN gives a slower speed for this shock. Second, in the SGN simulations, we

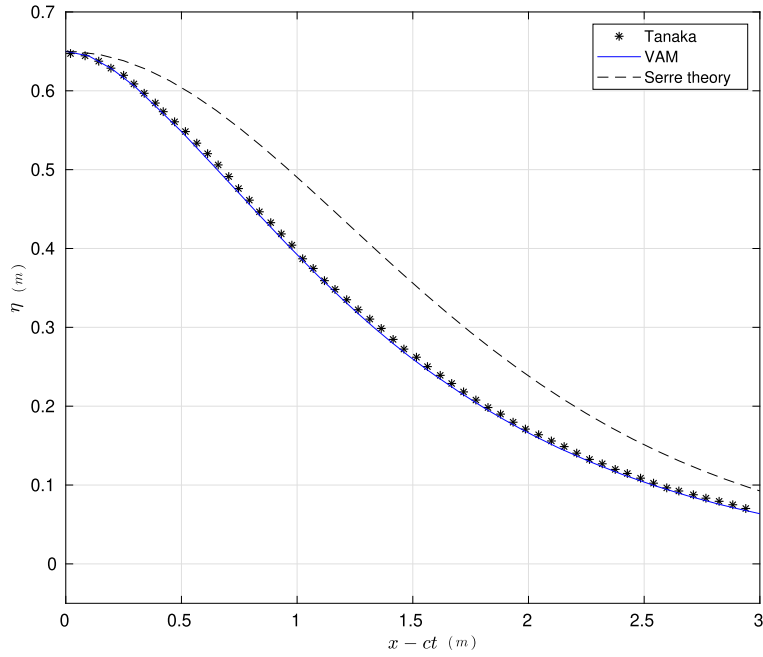


Fig. 7. Comparison between the vertically averaged and moment (VAM) equations, the Serre (1953) theory, and the Tanaka (1986) results for a large-amplitude solitary wave of amplitude $A = 0.65$ m.

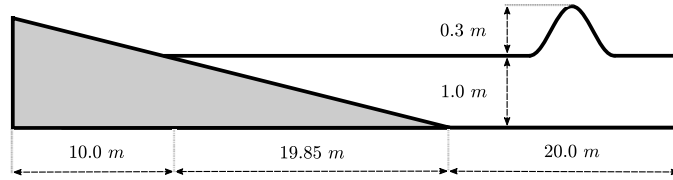


Fig. 8. Sketch of the topography.

see the characteristic overshoot in the surface. It is well-known that, in such situations, a breaking-wave mechanism is needed (see [24] and references therein). That is not the case for the VAM system, where breaking waves are correctly simulated without further treatment. We also remark that the run-up for SGN does not coincide with VAM.

If we compare the wall-clock times needed for each of them, they are similar: 3.261 s for SGN vs 3.464 s. Therefore, we see that the gain in the quality and precision of the solution for VAM are remarkable, with very little increase in computational effort.

4.5. Propagation of regular waves over submerged bar

The experiments described in [7,20], carried out in a wave flume with a submerged trapezoidal bar, is also a famous test case for phase-resolving models.

For this test, the spatial domain $[0, 30]$ m with a submerged trapezoidal obstacle is considered as in Fig. 11. The domain is covered with cells of the constant length of $\Delta x = 0.02$ m. An incident sinusoidal wave train for the free-surface η is imposed as a boundary condition at the left-hand side of the domain $x = 0$ m. That is done as in [25] setting:

$$\eta_{\ell}(t) = A \sin\left(\frac{2\pi}{T}t\right),$$

where $A = 0.01$ m and $T = 2.02$ s denote respectively amplitude and period. The rest of the flow variables at $x = 0$ m are imposed to be zero. At the right side of the domain, free-outflow boundary conditions are imposed. The generated wave train is measured in eight point stations G_1, G_2, \dots, G_8 for the free-surface η (Fig. 11).

Fig. 12 gives the results at the different gauge points. First, we see an excellent agreement for the VAM model with the experimental data. We remark that we recover similar observations stated in the literature, such as [50] where σ -coordinates are used, or [25] where an enhanced two-layer version of the non-hydrostatic pressure multilayer system $LDNH_0$ is used. The results in [19] with a three-parameter Green-Naghdi model optimized for uneven bottoms show the same level of agreement. Therefore, we can obtain excellent agreement with a model that does not need the calibration of parameters (such as [25] or [19]) nor the use of complex vertical discretizations [50].

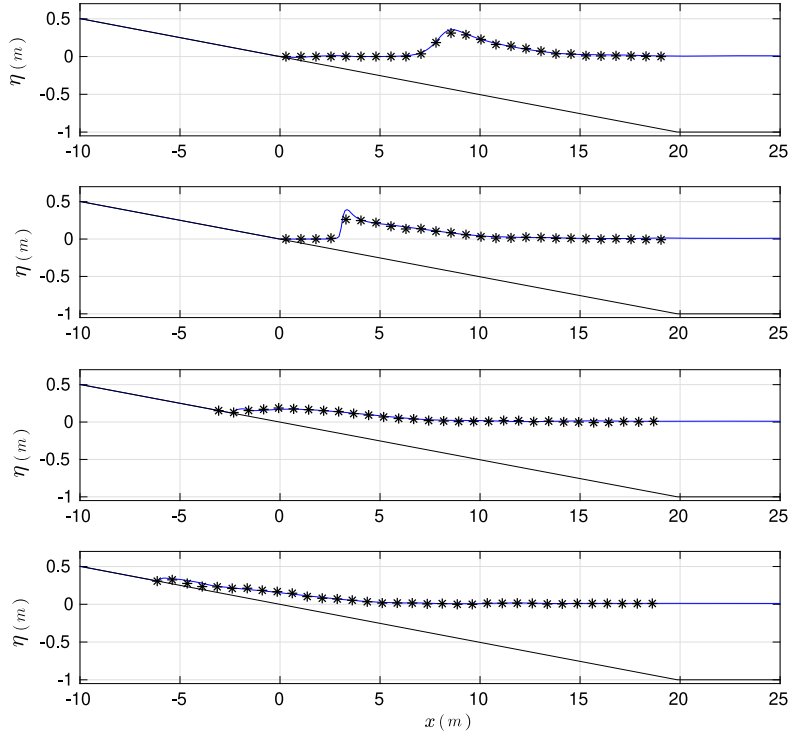


Fig. 9. Comparison of experimental data (star points) and simulated ones (solid lines) at times $t\sqrt{g/H} = 15, 20, 25, 30$.

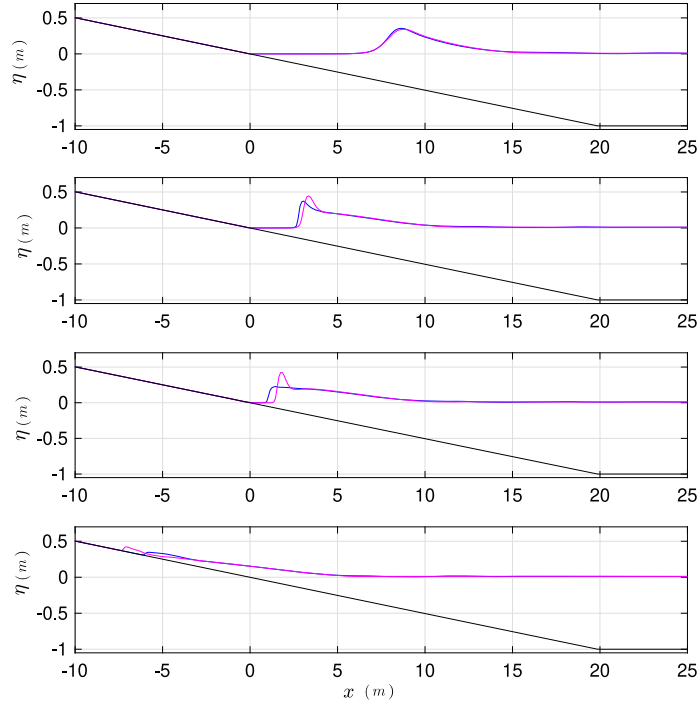


Fig. 10. Comparison VAM (blue) and SGN (magenta) surface evolution at times $t\sqrt{g/H} = 15, 20, 30, 21.87, 30$.

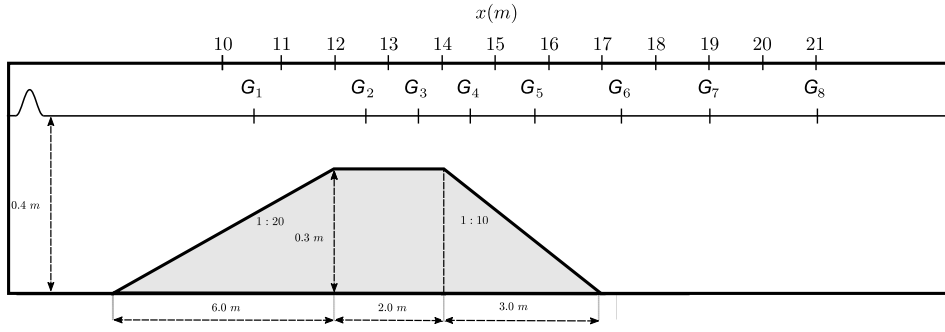


Fig. 11. Periodic waves breaking over a submerged bar. Sketch of the topography and layout of the wave gauges.

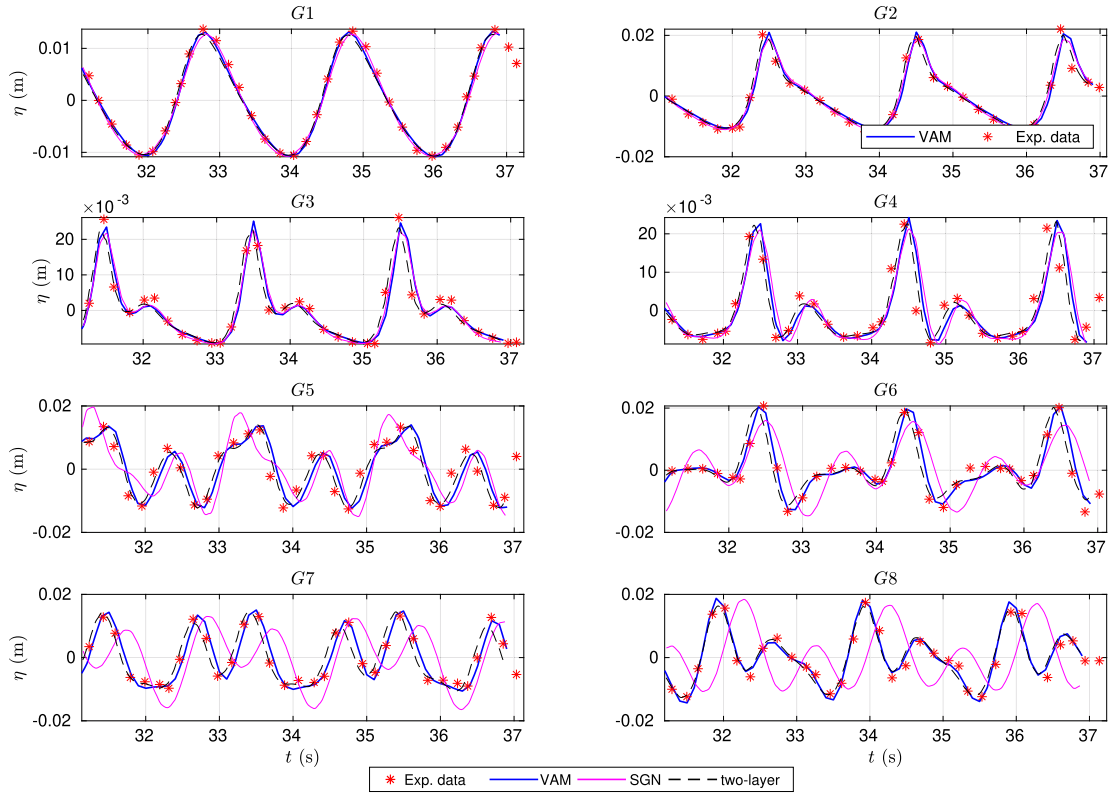


Fig. 12. Comparison of data time series (red star points) and numerical values at wave gauges G_1 , G_2 , G_3 , G_4 , G_5 , G_6 , G_7 , G_8 .

In the same figure, we also see the results obtained with SGN. The comparison with experimental data for gauge points after the submerged bar is not good. When comparing the wall-clock times for each system, VAM requires 62.694s while SGN needs 57.235s for the simulation. That means that the results are improved mainly with similar computational effort.

Moreover, to highlight the VAM model's performance, we also show the results obtained with the model $LDNH_0$ introduced in [25,26] for the case of two layers. The $LDNH_0$ is a multilayer non-hydrostatic model that tends to the dispersive relations provided by Airy linear theory as the number of layers increases. Of course, the counterpart of increasing the number of layers is that the computational cost also increases. In that case, we see that two layers are sufficient to obtain good results at all gauges. In particular, we see that VAM model fits experimental data and a two-layer model. Therefore, we obtain comparable results without the extra computational cost of increasing the number of layers.

Finally, a Fourier analysis was used to examine energy transfers among wave harmonics and the results are depicted in Fig. 13. The model overall reflects the evolution of the first six harmonics. The fundamental harmonic's amplitude ($f = 1/T$) decreases after $x = 10$ m as energy transfers to higher harmonics. Second harmonic ($2f$) increases until $x = 14$ m, then fluctuates. Higher harmonics develop around the bar crest ($x \in [12, 14]$ m). Harmonics $3f$ to $6f$ decrease after the bar, unlike $2f$ and $3f$. After the bar, $2f$ has the highest amplitude. The model aligns well with the data, with slight variations in the first and second harmonic's amplitudes at some locations, like $x = 16$ m.

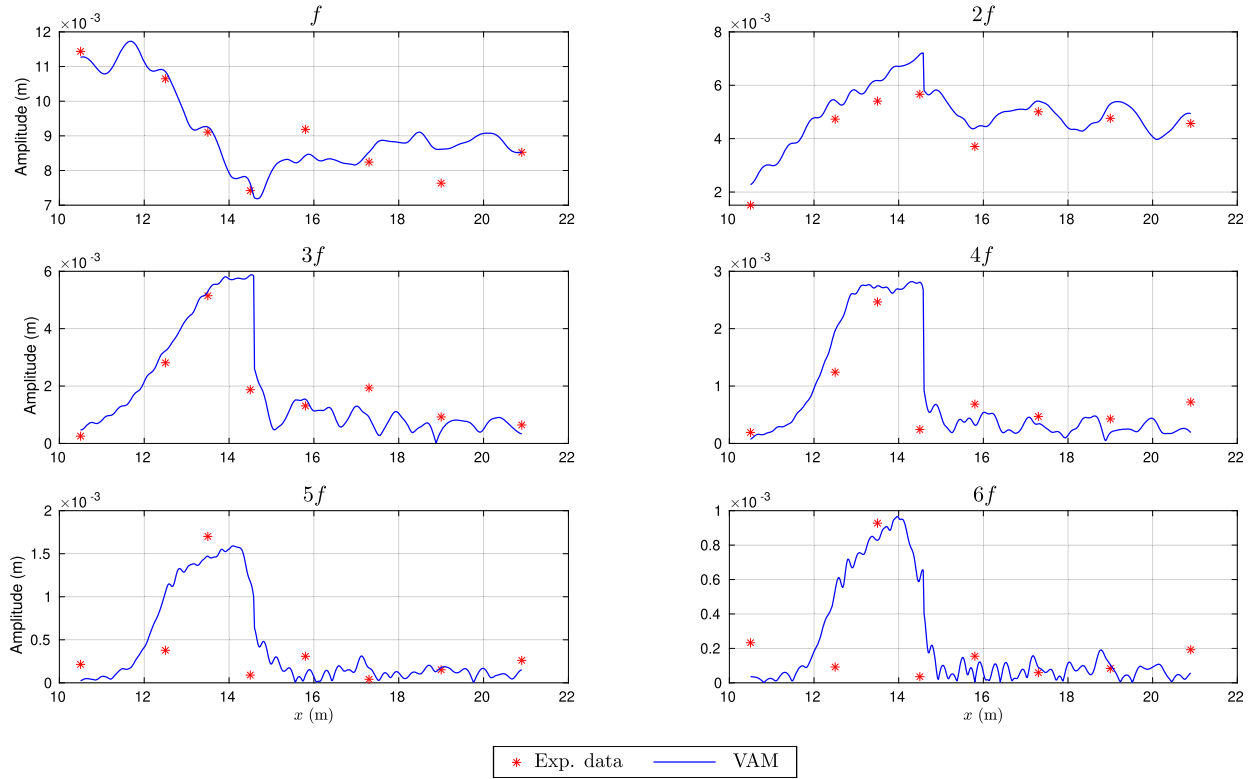


Fig. 13. Spatial evolution of the first six harmonic amplitudes (at frequencies $f = 1/T$, $2f$, ..., $6f$) of the free surface elevation experiments (red star points) and numerical simulation (solid blue lines).

4.6. Dam-break flood waves

With the subsequent two proposed numerical tests, we check the shock-capturing capabilities of the numerical model by considering a dam-break flood wave. Both situations will produce a rarefaction wave with an edge moving faster than the long-wave celerity and an undular shock front composed of a solitary-like leading wave and the second train of cnoidal-like called Favre waves. The experiments are described in [28,61], where a flume 15.24 m long, 0.4 m wide, and 0.4 m high is used.

For the first test case, the domain $[-10, 10]$ m is discretized with $\Delta x = 0.01$ m. The bottom is set to $b = 0$ m, and the water depth equals 0.1 m upstream and 0.045 m downstream, with the gate placed at $x = 0$ m. The rest of the flow variables are initially set to zero, open boundary conditions were imposed everywhere, and CFL is set to 0.4. Finally, no friction effects were considered here as they are not relevant for this test case.

Fig. 14 gives the corresponding results for the free surface. The results again agree with the experimental data: the rarefaction wave profile is well reproduced, and the shock front position is well predicted, especially at $t = 0.22$ s and $t = 0.32$ s. Nevertheless, the amplitude of the leading solitary-type wave of the bore front is overestimated for $t = 0.76$ s. We remark again that no empirical wave-breaking mechanism is considered here.

We further study the simulation of Favre waves generated in a laboratory flume using the experiments presented in [31,61]. The domain $[0, 30]$ is discretized using constant cells of $\Delta x = 0.01$ m length. The bottom is set to $b = 0$ m, and the water height is $h = 0.251$ m. The rest of the flow variables were initially set to zero. A bore with a Froude number $F = 1.104$, where

$$F^2 = \frac{h_u(h_u + h_d)}{2h_d^2},$$

was generated by imposing $h = 0.285989$ m on the left-hand side of the domain. Free-outflow boundary conditions for the rest of the flow variables were imposed everywhere.

The evolution of the undular bore was obtained for water level gauges positioned at the following distances from the gate placed at $x = 0$ m: C_0 ($x = 6.15$ m), C_1 ($x = 13.15$ m), C_2 ($x = 15.65$ m), C_3 ($x = 18.15$ m), C_4 ($x = 20.65$ m), and C_5 ($x = 23.15$ m).

Results are shown in Fig. 15 where inviscid computations show excellent agreement with experimental data for all water level gauges.

Finally, we include an analysis of the computational effort of two models, namely, the VAM model and the non-dispersive SW equations, applied to the first test case up to a simulated time of $t = 1$ s. The relevant information is summarized in Table 3, including the ratio between the computational effort of both models.

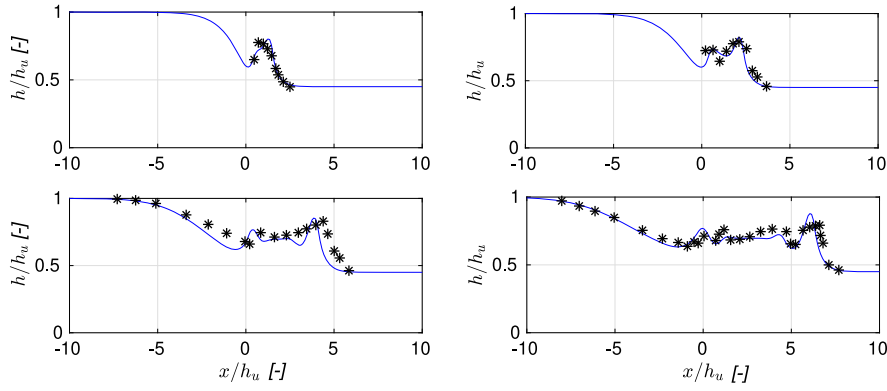


Fig. 14. Dam-break flow for at times $t = 0.22$ s (upper left), $t = 0.32$ s (upper right), $t = 0.52$ s (lower left), and $t = 0.76$ s (lower right).

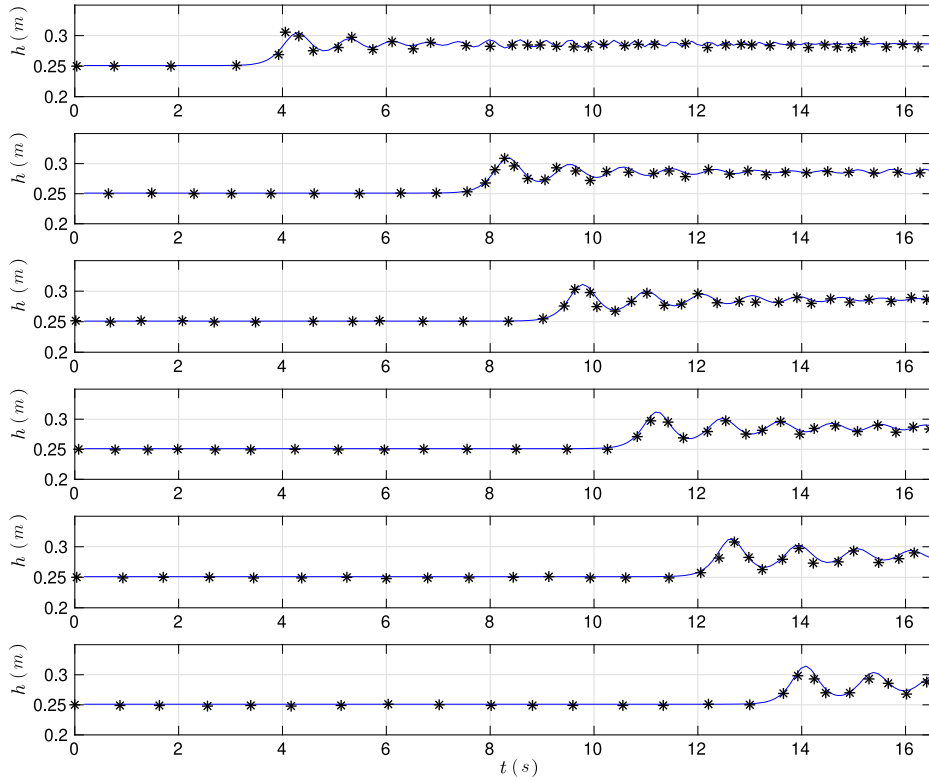


Fig. 15. Favre wave test for $F = 1.104$. Temporal evolution of water levels at gauges C_0 ($x = 6.15$ m), C_1 ($x = 13.15$ m), C_2 ($x = 15.65$ m), C_3 ($x = 18.15$ m), C_4 ($x = 20.65$ m), and C_5 ($x = 23.15$ m). Starred values correspond to experimental measurements, and blue solid lines correspond to numerical results.

Table 3 demonstrates that the VAM introduces a computational penalty compared to the simpler SW model. Specifically, this increase in computational effort ranges between 2 and 3.5 for typical and reasonable mesh size. As the mesh size is refined, an increase in this ratio is observed, which is an expected result due to the resolution of larger linear systems in the VAM model.

To the best of our knowledge, this work represents a significant advancement in the efficiency of the VAM model implementation compared to previous studies conducted by other researchers. For instance, in [13], computational effort ratios between 4.52 and 13.94 were reported for a similar test case with coarser meshes.

5. Conclusions

A new derivation of the VAM model using sigma-coordinates and a Galerkin procedure with shifted Legendre polynomials is presented. An efficient and new numerical approach to solve the ensuing vertically averaged and moment equations non-hydrostatic system (VAM model) is proposed. This numerical approach is based on a two-step algorithm: first, the hyperbolic part of the system is solved with a second-order path-conservative PVM scheme. Second, non-hydrostatic terms are corrected by solving a linear Poisson-

Table 3
Runtime in sec for VAM and SW models.

Δx	VAM	SW	Ratio
1.00e-2	0.65	0.31	2.10
5.00e-3	3.14	1.29	2.43
2.50e-3	16.20	5.27	3.07
1.25e-3	70.05	20.89	3.53

like system using an iterative method. The numerical approach has proven to be efficient, and the results are accurate and provide a good fit for experimental data. Moreover, compared to the well-known SGN system, the scheme described here and applied to the VAM system has a similar computational effort, while the results are largely improved. Furthermore, the results given by the VAM system are comparable to those obtained with a two-layer non-hydrostatic system while being less expensive from the computational point of view. Therefore, using the VAM system described in this work combined with the efficient numerical technique proposed is a reasonable choice in terms of computational effort and physical accuracy to deal with non-hydrostatic simulations of free surface flows.

CRedit authorship contribution statement

C. Escalante: Conceptualization, Methodology, Software, Validation, Writing – original draft, Writing – review & editing. **T. Morales de Luna:** Conceptualization, Methodology, Writing – review & editing. **F. Cantero-Chinchilla:** Data curation, Validation, Visualization, Writing – review & editing. **O. Castro-Orgaz:** Conceptualization, Validation, Writing – review & editing.

Declaration of competing interest

The authors declare the following financial interests/personal relationships which may be considered as potential competing interests: Cipriano Escalante reports financial support was provided by Ministry of Science, Innovation and Universities. Oscar Castro-Orgaz reports financial support was provided by Ministry of Science, Innovation and Universities.

Data availability

Data will be made available on request.

Acknowledgements

This work is partially supported by projects RTI2018-096064-B-C2(1-2), PID2020-114688RB-I00, and PID2022-137637NB-C21 funded by Ministry of Science, Innovation and Universities MCIN/AEI/10.13039/501100011033 and “ERDF A way of making Europe”. F. Cantero-Chinchilla was partially supported by the grant IJC2020-042646-I, funded by CIN/AEI/10.13039/501100011033 and by the European Union “NextGenerationEU/PRTR”, through the Spanish Ministry of Science, Innovation and Universities Juan de la Cierva program 2020.”

References

- [1] M.B. Abbott, A.D. McCowan, I.R. Warren, Accuracy of short-wave numerical models, *J. Hydraul. Eng.* 110 (10) (1984) 1287–1301.
- [2] M. Antuono, M. Brocchini, Beyond Boussinesq-type equations: semi-integrated models for coastal dynamics, *Phys. Fluids* 25 (1) (2013).
- [3] M. Antuono, G. Colicchio, C. Lugni, M. Greco, M. Brocchini, A depth semi-averaged model for coastal dynamics, *Phys. Fluids* 29 (5) (2017).
- [4] M. Antuono, A. Lucarelli, A. Bardazzi, M. Brocchini, A wave-breaking model for the depth-semi-averaged equations, *J. Fluid Mech.* 948 (2022).
- [5] N. Aïssiouene, M.-O. Bristeau, E. Godlewski, J. Sainte-Marie, A combined finite volume - finite element scheme for a dispersive shallow water system, *Netw. Heterog. Media* 11 (1) (2016) 1–27.
- [6] Y. Bai, K.F. Cheung, Depth-integrated free-surface flow with a two-layer non-hydrostatic formulation, *Int. J. Numer. Methods Fluids* 69 (2) (2011) 411–429.
- [7] S. Beji, J. Battjes, Numerical simulation of nonlinear wave propagation over a bar, *Coast. Eng.* 23 (1–2) (1994) 1–16.
- [8] K. Belibassakis, G. Athanassoulis, A coupled-mode system with application to nonlinear water waves propagating in finite water depth and in variable bathymetry regions, *Coast. Eng.* 58 (4) (2011) 337–350.
- [9] J. Boussinesq, Théorie des ondes et des remous qui se propagent le long d’un canal rectangulaire horizontal, en communiquant au liquide contenu dans ce canal des vitesses sensiblement pareilles de la surface au fond, *J. Math. Pures Appl.*, 2e Sér. 17 (1872) 55–108.
- [10] M.-O. Bristeau, A. Mangeney, J. Sainte-Marie, N. Seguin, An energy-consistent depth-averaged Euler system: derivation and properties, *Discrete Contin. Dyn. Syst.*, Ser. B 20 (4) (2015) 961–988.
- [11] J. Burguete, P. García-Navarro, J. Murillo, I. García-Palacín, Analysis of the friction term in the one-dimensional shallow-water model, *J. Hydraul. Eng.* 133 (9) (2007) 1048–1063.
- [12] F.N. Cantero-Chinchilla, O. Castro-Orgaz, A.A. Khan, Depth-integrated nonhydrostatic free-surface flow modeling using weighted-averaged equations, *Int. J. Numer. Methods Fluids* 87 (1) (2018) 27–50.
- [13] F.N. Cantero-Chinchilla, R.J. Bergillos, P. Gamero, O. Castro-Orgaz, L. Cea, W.H. Hager, Vertically averaged and moment equations for dam-break wave modeling: shallow water hypotheses, *Water* 12 (11) (2020).
- [14] F.N. Cantero-Chinchilla, R.J. Bergillos, O. Castro-Orgaz, Nearshore coastal flow processes using weighted-averaged equations, *Ocean Eng.* 211 (2020).
- [15] J.D. Carter, R. Cienfuegos, The kinematics and stability of solitary and cnoidal wave solutions of the Serre equations, *Eur. J. Mech. B, Fluids* 30 (3) (2011) 259–268.

- [16] M. Castro, J. Gallardo, C. Parés, High order finite volume schemes based on reconstruction of states for solving hyperbolic systems with nonconservative products. Applications to shallow-water systems, *Math. Comput.* 75 (255) (2006) 1103–1134.
- [17] M.J. Castro Díaz, E. Fernández-Nieto, A class of computationally fast first order finite volume solvers: PVM methods, *SIAM J. Sci. Comput.* 34 (4) (2012) A2173–A2196.
- [18] O. Castro-Organ, F.N. Cantero-Chinchilla, Non-linear shallow water flow modelling over topography with depth-averaged potential equations, *Environ. Fluid Mech.* 20 (2) (2019) 261–291.
- [19] F. Chazel, D. Lannes, F. Marche, Numerical simulation of strongly nonlinear and dispersive waves using a Green–Naghdi model, *J. Sci. Comput.* 48 (1) (2011) 105–116.
- [20] M. Dingemans, Comparison of computations with Boussinesq-like models and laboratory measurements, Report H-1684.12, 32, Delft Hydraulics, 1994.
- [21] A. Duran, F. Marche, Discontinuous-Galerkin discretization of a new class of Green–Naghdi equations, *Commun. Comput. Phys.* 17 (3) (2015) 721–760.
- [22] R.C. Ertekin, M. Hayatdavoodi, J.W. Kim, On some solitary and cnoidal wave diffraction solutions of the Green–Naghdi equations, *Appl. Ocean Res.* 47 (2014) 125–137.
- [23] C. Escalante, T. Morales de Luna, A general non-hydrostatic hyperbolic formulation for Boussinesq dispersive shallow flows and its numerical approximation, *J. Sci. Comput.* 83 (3) (2020) 62.
- [24] C. Escalante, T. Morales de Luna, M.J. Castro, Non-hydrostatic pressure shallow flows: GPU implementation using finite volume and finite difference scheme, *Appl. Math. Comput.* 338 (2018) 631–659.
- [25] C. Escalante, E.D. Fernández-Nieto, T. Morales de Luna, M.J. Castro, An efficient two-layer non-hydrostatic approach for dispersive water waves, *J. Sci. Comput.* 79 (1) (2019) 273–320.
- [26] C. Escalante, E.D. Fernández-Nieto, T. Morales de Luna, Y. Penel, J. Sainte-Marie, Numerical simulations of a dispersive model approximating free-surface Euler equations, *J. Sci. Comput.* 89 (3) (2021) 1–35.
- [27] C. Escalante, E. Fernández-Nieto, J. Garres-Díaz, Y. Penel, T. Morales de Luna, Non-hydrostatic layer-averaged approximation of Euler system with enhanced dispersion properties, *Comput. Appl. Math.* 42 (177) (2023).
- [28] H. Favre, Étude théorique et expérimentale des ondes de translation dans les canaux découverts, Publications du Laboratoire de Recherches Hydrauliques, Annexe à l'École Polytechnique Fédérale de Zurich, Dunod, 1935.
- [29] N. Favrie, S. Gavriluk, A rapid numerical method for solving Serre-Green-Naghdi equations describing long free surface gravity waves, *Nonlinearity* 30 (7) (2017) 2718–2736.
- [30] E.D. Fernández-Nieto, M. Parisot, Y. Penel, J. Sainte-Marie, A hierarchy of dispersive layer-averaged approximations of Euler equations for free surface flows, *Commun. Math. Sci.* 16 (5) (2018) 1169–1202.
- [31] S.S. Frazao, Y. Zech, Undular bores and secondary waves -experiments and hybrid finite-volume modelling, *J. Hydraul. Res.* 40 (1) (2002) 33–43.
- [32] P. Gamero, R.J. Bergillos, F.N. Cantero-Chinchilla, O. Castro-Organ, A MATLAB software platform for modelling vertically-integrated non-hydrostatic flows with moment equations, *Environ. Model. Softw.* 127 (2020) 104674.
- [33] J. Garres-Díaz, M.J. Castro Díaz, J. Koellermeier, T. Morales de Luna, Shallow water moment models for bedload transport problems, *Commun. Comput. Phys.* 30 (3) (2021) 903–941.
- [34] H.K. Ghamry, P.M. Steffler, Effect of applying different distribution shapes for velocities and pressure on simulation of curved open channels, *J. Hydraul. Eng.* 128 (11) (2002) 969–982.
- [35] H.K. Ghamry, P.M. Steffler, Two dimensional vertically averaged and moment equations for rapidly varied flows, *J. Hydraul. Res.* 40 (5) (2002) 579–587.
- [36] H.K. Ghamry, P.M. Steffler, Two-dimensional depth-averaged modeling of flow in curved open channels, *J. Hydraul. Res.* 43 (1) (2005) 44–55.
- [37] S. Gottlieb, C.-W. Shu, Total variation diminishing Runge-Kutta schemes, *Math. Comput.* 67 (221) (1998) 73–85.
- [38] A. Green, P. Naghdi, A direct theory of viscous fluid flow in channels, *Arch. Ration. Mech. Anal.* 86 (1) (1984) 39–63.
- [39] A.E. Green, P. Naghdi, Directed fluid sheets, *Proc. R. Soc. Lond. Ser. A, Math. Phys. Sci.* 347 (1651) (1976) 447–473.
- [40] A.E. Green, P.M. Naghdi, A derivation of equations for wave propagation in water of variable depth, *J. Fluid Mech.* 78 (2) (1976) 237–246.
- [41] A.E. Green, P.M. Naghdi, A nonlinear theory of water waves for finite and infinite depths, *Philos. Trans. R. Soc. Lond. Ser. A, Math. Phys. Sci.* 320 (1552) (1986) 37–70.
- [42] A.E. Green, P.M. Naghdi, Further developments in a nonlinear theory of water waves for finite and infinite depths, *Philos. Trans. R. Soc. Lond. Ser. A, Math. Phys. Sci.* 324 (1577) (1987) 47–72.
- [43] A. Harten, P.D. Lax, B. van Leer, On upstream differencing and Godunov-type schemes for hyperbolic conservation laws, *SIAM Rev.* 25 (1983).
- [44] L.V. Kantorovich, V.I. Krylov, Approximate Methods of Higher Analysis, Interscience Publishers, Inc., New York, 1958, P. Noordhoff Ltd., Groningen, translated from the 3rd Russian edition by C.D. Benster.
- [45] K. Kazhyken, J. Videman, C. Dawson, Discontinuous Galerkin methods for a dispersive wave hydro-morphodynamic model with bed-load transport, *Comput. Methods Appl. Mech. Eng.* 375 (2021) 113592.
- [46] M. Kazolea, A. Filippini, M. Ricchiuto, Low dispersion finite volume/element discretization of the enhanced Green-Naghdi equations for wave propagation, breaking and runoff on unstructured meshes, *Ocean Model.* 182 (2023) 102157.
- [47] H.P. Langtangen, G. Pedersen, Computational models for weakly dispersive nonlinear water waves, *Comput. Methods Appl. Mech. Eng.* 160 (3) (1998) 337–358.
- [48] D. Lannes, P. Bonneton, Derivation of asymptotic two-dimensional time-dependent equations for surface water wave propagation, *Phys. Fluids* 21 (1) (2009) 016601.
- [49] M. Li, P. Guyenne, F. Li, L. Xu, High order well-balanced CDG–FE methods for shallow water waves by a Green–Naghdi model, *J. Comput. Phys.* 257 (2014) 169–192.
- [50] G. Ma, F. Shi, J. Kirby, Shock-capturing non-hydrostatic model for fully dispersive surface wave processes, *Ocean Model.* 43 (2012) 22–35.
- [51] P.A. Madsen, O.R. Sørensen, A new form of the Boussinesq equations with improved linear dispersion characteristics. Part 2. A slowly-varying bathymetry, *Coast. Eng.* 18 (3) (1992) 183–204.
- [52] O.L. Métayer, S. Gavriluk, S. Hank, A numerical scheme for the Green-Naghdi model, *J. Comput. Phys.* 229 (6) (2010) 2034–2045.
- [53] D. Mitsotakis, B. Ilan, D. Dutykh, On the Galerkin/finite-element method for the Serre equations, *J. Sci. Comput.* 61 (1) (2014) 166–195.
- [54] O. Nwogu, Alternative form of Boussinesq equations for nearshore wave propagation, *J. Waterw. Port Coast. Ocean Eng.* 119 (6) (1993) 618–638.
- [55] C. Papoutsellis, A. Charalampopoulos, G. Athanassoulis, Implementation of a fully nonlinear hamiltonian coupled-mode theory, and application to solitary wave problems over bathymetry, *Eur. J. Mech. B, Fluids* 72 (2018) 199–224.
- [56] M. Parisot, Entropy-satisfying scheme for a hierarchy of dispersive reduced models of free surface flow, *Int. J. Numer. Methods Fluids* 91 (10) (2019) 509–531.
- [57] D.H. Peregrine, Long waves on a beach, *J. Fluid Mech.* 27 (4) (1967) 815–827.
- [58] A. Samii, C. Dawson, An explicit hybridized discontinuous Galerkin method for Serre-Green-Naghdi wave model, *Comput. Methods Appl. Mech. Eng.* 330 (2018) 447–470.
- [59] F. Serre, Contribution à l'étude des écoulements permanents et variables dans les canaux, *Houille Blanche* 39 (6) (1953) 830–872.
- [60] N.S. Sivakumaran, T. Tingsanchali, R.J. Hosking, Steady shallow flow over curved beds, *J. Fluid Mech.* 128 (1) (1983) 469.
- [61] S. Soares-Frazão, V. Guinot, A second-order semi-implicit hybrid scheme for one-dimensional Boussinesq-type waves in rectangular channels, *Int. J. Numer. Methods Fluids* 58 (3) (2008) 237–261.
- [62] P.M. Steffler, J. Yee-Chung, Depth averaged and moment equations for moderately shallow free surface flow, *J. Hydraul. Res.* 31 (1) (1993) 5–17.

- [63] G. Stelling, M. Zijlema, An accurate and efficient finite-difference algorithm for non-hydrostatic free-surface flow with application to wave propagation, *Int. J. Numer. Methods Fluids* 43 (1) (2003) 1–23.
- [64] M. Tanaka, The stability of solitary waves, *Phys. Fluids* 29 (3) (1986) 650.
- [65] V.V. Titov, C.E. Synolakis, Modeling of breaking and nonbreaking long-wave evolution and runup using VTCS-2, *J. Waterw. Port Coast. Ocean Eng.* 121 (6) (1995) 308–316.
- [66] B. van Leer, Towards the ultimate conservative difference scheme. V. A second-order sequel to Godunov's method, *J. Comput. Phys.* 32 (1) (1979) 101–136.
- [67] G. Wei, J.T. Kirby, S.T. Grilli, R. Subramanya, A fully nonlinear Boussinesq model for surface waves. Part 1. Highly nonlinear unsteady waves, *J. Fluid Mech.* 294 (1995) 71–92.
- [68] Y. Yamazaki, Z. Kowalik, K.F. Cheung, Depth-integrated, non-hydrostatic model for wave breaking and run-up, *Int. J. Numer. Methods Fluids* 61 (5) (2009) 473–497.
- [69] Z. Yang, P.L.-F. Liu, Depth-integrated wave–current models. Part 2. Current with an arbitrary profile, *J. Fluid Mech.* 936 (2022).
- [70] Z.T. Yang, P.L.-F. Liu, Depth-integrated wave–current models. Part 1. Two-dimensional formulation and applications, *J. Fluid Mech.* 883 (2019).
- [71] M.L. Yates, M. Benoit, Accuracy and efficiency of two numerical methods of solving the potential flow problem for highly nonlinear and dispersive water waves, *Int. J. Numer. Methods Fluids* 77 (10) (2015) 616–640.
- [72] J. Zhang, M. Benoit, Wave–bottom interaction and extreme wave statistics due to shoaling and de-shoaling of irregular long-crested wave trains over steep seabed changes, *J. Fluid Mech.* 912 (2021).
- [73] B. Zhao, W. Duan, R. Ertekin, Application of higher-level GN theory to some wave transformation problems, *Coast. Eng.* 83 (2014) 177–189.
- [74] B. Zhao, M. Li, W. Duan, R. Ertekin, M. Hayatdavoodi, An effective method for nonlinear wave–current generation and absorption, *Coast. Eng.* 185 (2023) 104359.